Electro-chemical polarization around metallic particles - Part 2: The role of diffuse surface charge

GEOPHYSICS®

Electro-chemical polarization around metallic particles - Part 2: The role of diffuse surface charge

Journal:	*Geophysics*
Manuscript ID	GEO-2018-0150.R2
Manuscript Type:	Technical Paper
Keywords:	induced polarization (IP), electrical/resistivity, rock physics, modeling, environmental
Area of Expertise:	Electrical and Electromagnetic Methods

ABSTRACT

Numerical simulations are carried out to study the induced-polarization response of a charged metallic sphere, which immersed in electrolyte solution is covered by a static diffuse layer. The metallic sphere itself is assumed to be perfectly conductive, electro-migration and diffusion processes in bulk electrolyte and diffuse layer are modelled by the Poisson-Nernst-Planck system of partial differential equations. To include the effect of a fixed diffuse charge, we consider a constant electric ζ-potential at the surface of the particle, which leads to the build-up of a static diffuse layer. Furthermore, a minor fraction of electro-active cations engages in oxidation-reduction reactions at the particle surface, which allows charges to be transferred across the solid-liquid interface. Upon excitation by a low-frequency electric field, we observe the coupling of three polarization processes in the composite material consisting of metallic particle and surrounding electrolyte. The first is related to the dynamic charging of field-induced diffuse layers immediately outside the two hemispheres of the sphere. The other two are volume-diffusion processes; (i) one driven by the reaction currents through the particle surface and (ii) the other by the unequal electro-migration transport of anions and cations through the static diffuse layer. Diffuse-layer relaxation and volume-diffusion due to reaction currents can also be observed around uncharged metallic particles and clearly dominate the macroscopic polarization response. The ζ-surface potential at the particle surface, and thus the static diffuse layer, only moderately change the relaxation of the field-induced diffuse layer: With increasing magnitude of the ζ-potential, we observe an increase of the low-frequency electrical conductivity of the particle in suspension, a reduction of its polarization magnitude and a shift of its characteristic frequency towards lower frequencies. The volume-diffusion process due to the reaction currents remains practically unaffected by the static diffuse layer.

INTRODUCTION

In a previous study (Bücker et al., 2018), we have presented the full analytical solution for the classical electrode-polarization model of the induced-polarization (IP) response of uncharged metallic particles proposed by Wong (1979). In the present paper, we extend this polarization model and develop a numerical scheme to study the response of charged metallic particles. The pre-charged surfaces of such particles immersed in an electrolyte solution are covered by static diffuse clouds of counter charges known as the diffuse part of the electric double layer (EDL) , which must not be confused with the field-induced diffuse layers caused by an external excitation. Neither the classical model by Wong (1979) nor the more recent numerical modelling study carried out by Abdulsamad et al. (2017) or the semiconductor-polarization models developed by Revil et al. (2015b) and Misra et al. (2016a) consider the effect of such a static diffuse charge. Although it was claimed to be the actual cause of the polarization response of highly conductive particles in the conceptual models proposed by Gurin et al. (2015) and Placencia-Gómez and Slater (2015), to date no mechanistic polarization model has been developed to describe the effect of a fixed surface charge – independently of whether it is located in the inner Stern layer or the outer diffuse layer.

Depending on the chemical composition and the concentration of the electrolyte, diffuse charges on the surfaces of pure metals and metal-bearing minerals vary over a wide range of positive and negative values. The potential drop across the diffuse layer, which can be approximated by the experimentally determinable ζ-potential at the plane of shear, is often used to parameterize the charge stored in the diffuse layer. The ζ-potential of metallic and metal-bearing surface ranges from values as low as -50 mV on stainless steel surfaces at 10

mM NaCl and pH 7 (Boulangé-Petermann et al., 1995) to +20 mV on pyrite at 1 mM KNO_3 and pH 6 (Reyes-Bozo et al., 2015). As these values differ significantly from zero, a possible effect of the corresponding static EDL over the polarization response of metallic particles should not simply be discarded a priori. Reversely, recent laboratory and field studies with metallic nano-particles (e.g. Joyce et al., 2012; Flores Orozco et al., 2015; Aal et al., 2017) indicate that it might be possible to use IP measurements to retrieve information on the in-situ chemical condition and reactivity of the surfaces of metallic particles (Shi et al., 2015), which is strongly correlated with the ζ-potential.

It is the objective of the present study to develop a model, which describes the polarization response due to a static diffuse layer covering the surface of the metallic particles, and study the effect of varying charge densities in this layer. Our theoretical treatment is based on a modification of the system of partial differential equations proposed by Wong (1979) and therefore also permits to include the effect of reaction currents through the metal-electrolyte interface. As to our best knowledge the modified problem, which includes the polarization response of a static diffuse layer, cannot be solved analytically, we adopt a finite-element approach to obtain a numerical solution. Our results comprise the micro-scale perturbations of ion concentrations and electrical potential around the particle as well as the effect of the static diffuse layer on the effective electrical conductivity spectra of the composite system. Here, we focus on the impact of the diffuse charge on relevant descriptive parameters such as direct-current (DC) conductivity, relaxation time, and maximum polarization response. In the discussion section, we further analyze the practical relevance of our findings and implications for the interpretation of IP measurements.

THEORY

The electro-chemical polarization model introduced by Wong (1979) and Wong and Strangway (1981) describes the IP response of metal-bearing ores based on the frequency-dependent complex conductivity of perfectly conducting particles (e.g., metallic conductors) immersed in an electrolyte solution. As discussed in detail in Bücker et al. (2018), the primary polarization phenomenon inherent to this model is related to the dynamic charging of field-induced diffuse layers at the particle surface (see Bazant et al., 2004, for a comprehensive discussion of diffuse-charge dynamics). This mechanism does not require the presence of electro-active ions to establish. Rather, electro-active ions additionally allow reaction currents to cross the solid-liquid interface and trigger a volume-diffusion mechanism, which largely changes the polarization response particularly around larger particles.

Fundamental equations and extended model

Like Wong (1979), we consider a perfectly conducting sphere immersed in an electrolyte solution that consists of three ionic species. The supporting electrolyte consists of anions (subscript 1) and inactive cations (subscript 2), which do not engage in electrochemical reactions at the particle surface (e.g. Cl^- and Na^+). A smaller fraction of active cations (subscript 3), in contrast, does participate in reduction and oxidation reactions at the metallic surface, which allows a net electric current to cross the solid-liquid interface. Upon excitation by the uniform electric field $\mathbf{E}_{\text{ext}} = \mathbf{E}_0 e^{i\omega t}$, where ω and t denote angular frequency and time, respectively, the electric potential U and the ion concentrations n_j (in mol/m^3) around the particle will be perturbed from their equilibrium values. In three-dimensional coordinates, the total ion flux densities caused by the external excitation are

described by the Nernst-Planck equations (Nernst, 1888, 1889; Planck, 1890)

$$\mathbf{J}_j(\mathbf{r},t) = -D_j \nabla n_j(\mathbf{r},t) - \mu_j z_j n_j(\mathbf{r},t) \nabla U(\mathbf{r},t), \tag{1}$$

where D_j, μ_j, and z_j denote diffusion coefficient, mobility, and signed valence of the j-th ionic species. The first term on the right-hand side of equation 1 describes a diffusion current, while the second term corresponds to a conduction or electro-migration current. For the sake of simplicity, we limit our treatment to monovalent ions of symmetric electrolytes, i.e., $z_1 = -1$ and $z_2 = z_3 = 1$. Assuming, furthermore, the conservation of each ionic species expressed by the continuity equation $\nabla J_j(\mathbf{r},t) = -\partial_t n_j(\mathbf{r},t)$, equation 1 becomes

$$\partial_t n_j(\mathbf{r},t) = \nabla \left[D_j \nabla n_j(\mathbf{r},t) + \mu_j z_j n_j(\mathbf{r},t) \nabla U(\mathbf{r},t) \right]. \tag{2}$$

We use the compact notation $\partial_x f := \partial f / \partial x$ for partial derivatives with respect to x. The three ion concentrations are coupled amongst each other and to the total electric potential via Poisson's equation

$$\nabla^2 U(\mathbf{r},t) = -\frac{F}{\varepsilon_0 \varepsilon_r} \sum_{j=1}^{3} z_j n_j(\mathbf{r},t), \tag{3}$$

where $F = 96,485$ C/mol is Faraday's constant, $\varepsilon_0 = 8.85 \cdot 10^{-12}$ C/(Vm) the vacuum permittivity, and ε_r the constant relative permittivity of the aqueous electrolyte. The system of partial differential equations described by equations 2 and 3 is also known as the Poisson-Nernst-Planck (PNP) system for ion transport.

Following the treatment by Wong (1979), we decompose the concentration of the j-th ionic species into a static background concentration $n_j^{(0)}(\mathbf{r})$ and a perturbation $\delta n_j(\mathbf{r})$ imposed by the oscillating external field.

$$n_j(\mathbf{r},t) = n_j^{(0)}(\mathbf{r}) + \delta n_j(\mathbf{r}) \cdot e^{i\omega t} \tag{4}$$

In a similar fashion, the total electric potential can be decomposed into the background potential $U^{(0)}(\mathbf{r})$ and a perturbation potential $\delta U(\mathbf{r})$ as follows:

$$U(\mathbf{r},t) = U^{(0)}(\mathbf{r}) + \delta U(\mathbf{r}) \cdot e^{i\omega t} \tag{5}$$

Unlike in Wong's model, the background concentration $n_j^{(0)}(\mathbf{r})$ is not equal to the bulk concentration n_j^{∞} but includes the excess and defect concentrations caused by a fixed diffuse charge density at the particle surface. For the same reason, the background potential $U^{(0)}(\mathbf{r})$ can no longer be assumed to be zero as done in Wong's model.

Besides the differentiation between active and passive cations made here, equations 2 through 5 are essentially the same as used e.g. by Chew and Sen (1982b,a) to describe ion transport through the electrolyte around a charged particle. Although these authors model the polarization response of non-conducting particles, the physics controlling the response of the electrolyte solution is identical. The fundamentally different electrical characteristics of the suspended particles (non-conducting vs. perfectly conducting) are later taken into account by imposing appropriate boundary conditions at the particle surface.

According to these authors, the problem can be decomposed into the solution of a static part of the problem, which essentially yields the equilibrium ion concentrations $n_j^{(0)}(\mathbf{r})$ and electric potentials $U^{(0)}(\mathbf{r})$ in the static diffuse layer and the bulk electrolyte (Chew and Sen, 1982b), and the solution of a frequency-dependent part (Chew and Sen, 1982a), which yields the perturbation quantities $\delta n_j(\mathbf{r})$ and $\delta U(\mathbf{r})$ caused by the external excitation. While the static part does not depend on the perturbation quantities, the frequency-dependent solution couples to the static solution. Both parts of the solution are introduced in the following two subsections.

Static solution

In a variation of the approach by Chew and Sen (1982b,a), in absence of an external field, i.e for $\delta n_j(\mathbf{r}) = 0$ for all j and $\delta U(\mathbf{r}) = 0$, we write (from equation 2)

$$0 = \nabla \left[D_j \nabla n_j^{(0)}(\mathbf{r}) + \mu_j z_j n_j^{(0)}(\mathbf{r}) \nabla U^{(0)}(\mathbf{r}) \right]. \tag{6}$$

We assume that in equilibrium, i.e., without an external excitation, all three ion current densities through the particle surface vanish. This is obvious for the inactive ionic species, which do not penetrate the particle surface by definition, and also sensible for the active cations (see appendix A for more details). Under this condition, equation 6 is solved by the Boltzmann-distributed concentrations (e.g. Chew and Sen, 1982b)

$$n_j^{(0)}(\mathbf{r}) = n_j^{\infty} \exp\left(-\frac{z_j e}{kT} U^{(0)}(\mathbf{r}) \right), \tag{7}$$

where e denotes the elementary charge ($1.602 \cdot 10^{-19}$ C), k Boltzmann's constant ($8.617 \cdot 10^{-5}$ eV/K), and T the absolute temperature. The spatial variation of the static background potential $U^{(0)}(\mathbf{r})$ is coupled to the space charge resulting from equation 7 via Poisson's equation (from equation 3)

$$\nabla^2 U^{(0)}(\mathbf{r}) = -\frac{F}{\varepsilon_0 \varepsilon_r} \sum_{j=1}^{3} z_j n_j^{(0)}(\mathbf{r}). \tag{8}$$

Inserting equation 7 into 8 gives the well-known Poisson-Boltzmann equation, which together with the boundary conditions at the particle surface,

$$U^{(0)}(\mathbf{r})\Big|_{\text{surface}} = \zeta, \tag{9}$$

and at a far distance from the particle

$$U^{(0)}(\mathbf{r}) \xrightarrow[r \to \infty]{} 0, \tag{10}$$

determines the static background potential. Note that we placed the origin of our coordinate system ($r = 0$) in the centre of the metallic particle.

Because the static boundary conditions, i.e., equations 9 and 10, are the same as those used to describe the diffuse layer around a non-conducting particle, an approximate solution of the static potential $U^{(0)}(\mathbf{r})$ can be looked up in Chew and Sen (1982b) and inserted into equation 7 to obtain the static concentrations $n_j^{(0)}(\mathbf{r})$. Nevertheless, because the frequency-dependent solution requires the use of numerical methods, in the present study we will solve the static problem numerically, too.

Frequency-dependent solution

The static solution can then be used to obtain the perturbation potential $\delta U(\mathbf{r})$ and the perturbation ion concentrations $\delta n_j(\mathbf{r})$. Assuming that the amplitude $E_0 = |\mathbf{E}_0|$ of the external field is small (i.e., $E_0^2 \ll E_0$), all perturbation quantities are approximately proportional to the external excitation E_0. Extending the approach by Chew and Sen (1982a) to the case of three ionic species, the linearized frequency-dependent part of equation 2 writes

$$i\omega\delta n_j(\mathbf{r},\omega) = \nabla\Big\{ D_j\nabla\delta n_j(\mathbf{r},\omega) + \mu_j z_j \left[n_j^{(0)}(\mathbf{r})\nabla\delta U(\mathbf{r},\omega) + \delta n_j(\mathbf{r},\omega)\nabla U^{(0)}(\mathbf{r}) \right] \Big\} + \mathcal{O}(E_0^2), \quad (11)$$

where the term $\mathcal{O}(E_0^2)$ represents the neglected products of two perturbation quantities, and the perturbation potential satisfies Poisson's equation:

$$\nabla^2\delta U(\mathbf{r},\omega) = -\frac{F}{\varepsilon_0\varepsilon_r}\sum_{j=1}^{3} z_j\delta n_j(\mathbf{r},\omega). \quad (12)$$

Equations 11 and 12 constitute four coupled differential equation that describe the variation of the perturbation quantities within the electrolyte and it only remains to specify suitable boundary conditions. At a distance far from the particle, the perturbation potential should approach values corresponding to the external electric field, i.e.,

$$\delta U(\mathbf{r},\omega) \xrightarrow[r\to\infty]{} -\mathbf{E}_{\text{ext}} \cdot \mathbf{r}, \tag{13}$$

while the ion concentrations should approach the static solution, i.e., the perturbation concentrations should vanish as described by

$$\delta n_j(\mathbf{r},\omega) \xrightarrow[r\to\infty]{} 0. \tag{14}$$

We will assume that the particle can be considered a perfect conductor, such that the perturbation potential must be constant along the particle surface (see discussion section for a more detailed analysis of this assumption). If the external excitation is symmetric around the sphere, this constant potential must be zero, i.e.,

$$\delta U(\mathbf{r},\omega)\Big|_{\text{surface}} = 0. \tag{15}$$

As inactive ions are neither produced nor consumed at the particle surface, the normal fluxes of both inactive ionic species through the surface, i.e., equation 1 for $j = 1, 2$, must also be zero:

$$\left[-D_j \nabla \delta n_j(\mathbf{r},\omega) - \mu_j z_j \left(n_j^{(0)}(\mathbf{r},\omega) \nabla \delta U(\mathbf{r},\omega) + \delta n_j(\mathbf{r},\omega) \nabla U^{(0)}(\mathbf{r},\omega) \right) \right] \cdot \mathbf{n}\Big|_{\text{surface}} = 0, \tag{16}$$

with $\mathbf{n}$ denoting the unit normal vector to the surface (pointing into the electrolyte). Only the normal flux of the active cations through the metal surface is non-zero due to the oxidation-reduction reactions. The rate of ion production or consumption at the surface depends on the perturbation concentration of the active ions and the electric field at the

surface as expressed by

$$\left[-D_3\nabla\delta n_3(\mathbf{r},\omega) - \mu_3\left(n_3^{(0)}(\mathbf{r},\omega)\nabla\delta U(\mathbf{r},\omega) + \delta n_3(\mathbf{r},\omega)\nabla U^{(0)}(\mathbf{r},\omega)\right)\right]\cdot\mathbf{n}\Big|_{\text{surface}} = \\ -\alpha(\zeta)n_3^{(0)}(\mathbf{r},\omega)\nabla\delta U(\mathbf{r},\omega)\cdot\mathbf{n} - \beta(\zeta)\delta n_3(\mathbf{r},\omega), \quad (17)$$

where we already made use of the equality $z_3 = 1$. As we show in more detail in appendix A, the right-hand side of equation 17 corresponds to the exchange current across the metal electrolyte interface defined by Wong (1979) adapted to our extended model. The two parameters α (in Cs/kg) and β (in m/s) control the dependence of the reaction current on the overpotential at the particle surface and the perturbation of the active ion concentration, respectively. Details on the exchange current can be found in Appendix A. In the same appendix, we show that — assuming a constant reaction-current density i_0 — the two reaction-current parameters vary with the ζ-potential as follows:

$$\alpha(\zeta) = \alpha(0)\exp\left(\frac{e\zeta}{kT}\right), \quad \beta(\zeta) = \beta(0)\exp\left(\frac{e\zeta}{kT}\right), \quad (18)$$

where $\alpha(0)$ and $\beta(0)$ describe the reaction current in absence of a static surface potential as used in the study by Wong (1979). Note that in our case, the reaction current is given in terms of an ion flux density in mol/(m^{2}s), which has to be multiplied by Faraday's constant F to obtain the corresponding electric current density in A/m^2 as defined by Wong (1979) [his equation (28)].

NUMERICAL IMPLEMENTATION

To our best knowledge, no closed analytical solution of the problem set up by the partial differential equations 11 and 12 and the boundary conditions expressed in equations 13 through 17 exists in the literature. This is also true for similar systems of partial differential

equations with boundary conditions adjusted to the problem of charged non-conducting particles, for which only approximate analytical (e.g. Chew and Sen, 1982a; Shilov et al., 2001) or numerical solutions (e.g. DeLacey and White, 1981) have been reported.

Here, we use the finite-element software package COMSOL Multiphysics to successively obtain the static and the frequency-dependent solution. Although the numerical solution would also permit to study irregularly shaped particles, here we limit our treatment to spherical particles. This enables us to compare our results for the charged particle with the predictions of the analytical Wong model for an uncharged particle of equal size. Figure 1 illustrates the modelled volume with the particle of radius a centered at the origin of coordinates. The uniform external field is imposed, such that $\mathbf{E}_0 = E_0\mathbf{e}_x$.

Due to the cylindrical symmetry of the problem, the numerical simulation only needs to be carried out on the two-dimensional model domain of length $2L$ (in x-direction) and height L (in y-direction) marked in red in Figure 1. This approach, which helps to solve the numerical problem efficiently, is based on taking the x-coordinate of the Cartesian space as the z-coordinate of the cylindrical coordinate system and the y-coordinate as the radial coordinate r. As the problem is completely symmetric around the x- or z-axis, there is no variation in azimuthal direction. Additionally, this approach requires a suitable coordinate transformation, which accounts for the different form of the differential operators in cylindrical coordinates (see Appendix B for details).

As we saw earlier, in the case of vanishing equilibrium reaction current densities, the static problem reduces to the solution of the Poisson-Boltzmann equation, which contains $U^{(0)}(\mathbf{r})$ as only unknown variable. The boundary conditions, equations 9 and 10, are translated into the following boundary conditions for the numerical simulation: $U^{(0)} = \zeta$ on

the particle surface; $U^{(0)} = 0$ on the left, right, and top boundary (see Figure 1); and $\partial_y U(0) = 0$ on the axis of symmetry. For technical details on the implementation in COMSOL Multiphysics, see appendix B.

Because bulk values are imposed as boundary conditions on the left, right, and top boundary, these should be placed sufficiently far away from the static diffuse layer and the frequency-dependent induced perturbations around the particle. As a trade-off between computational cost and accuracy, we use a standard domain size L of four times the particle radius, i.e. $L = 4a$. We checked the suitability of this length scale by comparing the modelled perturbation potential at the boundary (for $\zeta = 0$) with the corresponding values of the analytical solution (Wong, 1979; Bücker et al., 2018). As our modelling results do not yield a longer-scale perturbation caused by the effect of the static diffuse layer (see next section), this criterion will turn out to be sufficient.

Furthermore, the discretization of the two-dimensional modelling domain should account for the expected small-scale variation of the solution within the diffuse layer at the particle surface. While particle sizes of at least 1 mm may be of interest, the thickness of the diffuse layer is only of the order of one Debye length

$$\lambda_D = \left(\frac{\varepsilon_0 \varepsilon_r kT}{2 n_1^\infty e F} \right)^{1/2}, \tag{19}$$

which for typical ionic strengths of the electrolyte is as small as 10^{-8} m. In order to be able to resolve the diffuse layer, we therefore discretizise the electrolyte next to the surface with a special boundary-layer mesh consisting of rectangular elements with a size of $\pi a/400$ along the boundary (tangential direction). In radial direction this boundary-layer mesh is much finer and consists of a fixed number of 8 elements with sizes increasing from $\lambda_D/2$ at the surface to $\approx 1.8\lambda_D$ at the outer limit of the boundary layer. The remaining volume is filled

with triangular elements, the maximum sizes of which increase from $\lambda_D/2$ at the outer limit of the boundary-layer mesh to $L/20$ at the remote boundaries. Resulting meshes consist of $\approx 9,250$ elements for particle sizes between 0.1 μm and 10 mm, of which the constant number of $3,200$ elements corresponds to the boundary-layer mesh.

After having solved the static problem, the frequency-dependent solution is obtained using the same mesh. The static background ion concentrations needed for the frequency-dependent solution, are computed by inserting $U^{(0)}(\mathbf{r})$ into equation 7. For the detailed implementation of the partial differential equations 11 through 12 in COMSOL Multiphysics, see appendix B. The analytical boundary conditions for the frequency-dependent problem, equations 13 through 17, merge into the following numerical formulation: Unchanged on the particle surface; $\delta n_j = 0$ for all j and $\delta U = \pm E_0 L$ on the left and right boundary, respectively; $\mathbf{J}_j = 0$ for all j and $\partial_y \delta U$ on the top boundary and the axis of symmetry. While the static solution only needs to be computed once for each set of model parameters (i.e., a, ζ, n_j^∞, etc.), the frequency-dependent problem has to be solved for each value of the angular frequency ω separately.

Further below, we will display the modelling results either directly, i.e., the actual solutions for the four perturbation quantities, or in terms of the effective conductivity of the modelled volume. The latter can be obtained from a numerical integration of the total ionic fluxes through the left (or right) boundary, i.e.,

$$\sigma_{\text{mod}} = \frac{2}{E_0 L^2} \int_0^L \sum_{j=1}^{3} \mathbf{J}_j(x = L, y)\mathbf{e}_x y dy, \tag{20}$$

where the term ydy accounts for the area element of the circular surface of the boundary and the factor $2/L^2$ stems from the normalization to its total area.

As mentioned above, the standard domain size is $L = 4a$ to ensure that the boundaries

are located far enough from the polarized particle. However, this corresponds to a rather small particle volume fraction of $\nu_{\mathrm{mod}} \approx 0.01$. In order to facilitate the comparison with the spectral responses discussed in Part 1 of this series (Bücker et al., 2018), the modelled effective conductivities σ_{mod} are scaled to the volumetric content of $\nu = 0.12$ using the Maxwell-Garnett mixing rule (e.g. Wong, 1979)

$$\frac{\sigma_{\mathrm{eff}}}{\sigma_0} = \frac{1 + 2\nu f}{1 - \nu f}, \tag{21}$$

where $\sigma_0 = 2\mu n_1^\infty F$ is the bulk conductivity of the electrolyte and

$$f = \frac{1}{\nu_{\mathrm{mod}}} \frac{\sigma_{\mathrm{mod}} - \sigma_0}{\sigma_{\mathrm{mod}} + 2\sigma_0} \tag{22}$$

the modelled frequency-dependent reflection coefficient of the spherical particle.

Due to the lack of an appropriate analytical model, the numerical solution around the charged particle itself cannot be validated rigorously. However, for the limiting case of a particle without diffuse charge, i.e., $\zeta = 0$, the numerical solution can be compared to the analytical solutions provided by Wong (1979) and Bücker et al. (2018) in order to detect possible problems due to an inappropriate discretization or other issues arising from the numerical implementation. In the results section, all numerical results are therefore presented along with the corresponding analytical solutions for an uncharged particle.

RESULTS

Unless otherwise stated, the standard model parameters listed in Table 1 are used to obtain the results presented in this section. As mentioned above, all numerical results are scaled to a standard volumetric content of 12%, which ensures a significant spectral variation of the effective conductivity. The ζ-potential on the surface of the charged particle is

set to $\zeta = -50$ mV, which is a typical value for stainless steel surfaces at neutral pH (Boulangé-Petermann et al., 1995) and high enough to render the small changes of the spectral response induced by the static diffuse layer visible. In a similar fashion, we use a relatively high bulk concentration of the active cations of $n_3^\infty = 0.12$ mol/m^3 to also highlight the effect of the reaction current. The values of the reaction current parameters $\alpha(0)$ and $\beta(0)$ for the uncharged particle are taken over from Wong (1979). A uniform ion mobility of $\mu_1 = \mu_2 = \mu_3 = \mu = 5 \cdot 10^{-8}$ m^2/(Vs), which is approximately the mobility of the sodium cation at room temperature (e.g. Atkins and De Paula, 2013), is assumed for all three ionic species.

Polarization mechanism

In part 1 (Bücker et al., 2018), we analyzed the two main relaxation processes inherent to Wong's electro-chemical polarization model: The first is related to the accumulation and relaxation of electrical charges in thin diffuse layers induced next to the two hemispheres of the particle. This dynamic charging relaxes on a characteristic time scale that increases linearly with the particle radius as $\tau_{\mathrm{dl}} = a\lambda_D/(2D)$. The second is a volume-diffusion process related to the build-up of an electrically neutral concentration gradient around the particle. This gradient is required to balance reaction currents through the particle and is therefore only observed in the presence of active cations (i.e., $n_3^\infty > 0$) and a non-zero exchange current (i.e., $\alpha(0), \beta(0) > 0$) at the particle surface. The relaxation of the concentration gradient occurs on a time scale $\tau_{\mathrm{vd}} \propto a^2/D$ and becomes dominant around particles with radius $8\lambda_D(n_1^\infty/n_3^\infty)^2$ or larger (see Bücker et al., 2018).

Figures 2 to 5 give an insight into the micro-scale manifestations of both mechanisms and

Table 1: Standard parameter values for numerical modelling studies.

Parameter (unit)	**Symbol**	**Value**
Absolute temperature (K)	T	293
Volumetric metal content (-)	ν	0.12
Particle radius (μm)	a	0.1
ζ-Potential (mV)	ζ	-50
Relative permittivity of the fluid (-)	ε_r	80
Ion mobility [$m^2/(Vs)$]	μ	$5 \cdot 10^{-8}$
Signed ion valences (-)	z_1, z_2, z_3	-1, 1, 1
Bulk anion concentration (mol/m^3)	n_1^∞	1
Bulk concentration of active cations (mol/m^3)	n_3^∞	0.12
Reaction-current parameter [$m^2/(Vs)$]	$\alpha(0)$	10^{-10}
Reaction-current parameter (m/s)	$\beta(0)$	10^{-2}
Magnitude of external field (V/m)	E_0	1

the changes produced by adding a static diffuse layer. The first row of Figure 2 shows the (purely radial) variation of the background ion concentrations $n_j^{(0)}(\mathbf{r})$ and the background potential $U^{(0)}(\mathbf{r})$ within such a static diffuse layer around a charged sub-micron particle with a radius of 0.1 μm and a ζ-potential of -50 mV. The dashed line indicates the approximate thickness $\lambda_D \approx 10$ nm of the diffuse layer. While the negative charges at the particle surface deplete anions (co-ions) almost completely from the diffuse layer, they increase both cation concentrations (counter-ions) at the surface by a factor of ≈ 7.2. Because the excess of

counter-ions outnumbers the deficit of co-ions, the effective conductivity of the interfacial layer is larger than the one of the bulk electrolyte. Outside the diffuse layer, all three ion concentrations approach their respective bulk concentrations and the static potential decays to 0 mV.

The other four rows of Figure 2 show particles of the same size (0.1 μm) but with different surface characteristics under the influence of an external field. The selected angular frequency of $\omega = 3 \cdot 10^4$ rad/s of the external excitation is well below the characteristic frequencies of all relaxations of interest, such that the corresponding perturbations can fully develop. Figure 2 displays the real parts of the complex-valued perturbation quantities. The corresponding imaginary parts are not displayed because they are much (at least by a factor of 10) smaller at the selected low angular frequency.

Complex-valued concentrations and potentials might be less familiar to some readers. But in the mathematical formalism used here, which describes harmonic oscillations by complex numbers, the occurrence of non-zero imaginary parts simply indicates that these quantities are out-of-phase compared to the external electrical field, the phase of which is given by the product ωt.

Upon excitation by the external field, the perfectly conducting sphere always responds with an quasi-instantaneous redistribution of charges along its surface. The resulting induced surface charges $\Sigma_\infty \propto \varepsilon_0 \varepsilon_r 3 E_0$ (see e.g. Bücker et al., 2018) ensure that the external field is cancelled out within the particle, which is being accounted for by the boundary condition 15. This early-time or high-frequency behaviour of the particle itself is the same, regardless of reaction currents through the particle surface or the assumption of a fixed diffuse surface charge. However, due to slower processes the variation of the late-time or

low-frequency perturbations of ion concentrations and electric potentials within the electrolyte next to the particle depends largely on the particular set of surface properties. In the following we will discuss the different effects of ζ-potential and reaction currents in detail.

The second row of Figure 2 and the solid grey curves in Figures 3 and 4 illustrate the low-frequency polarization of the uncharged conducting particle, i.e., $\zeta = 0$, with no reaction currents through the solid-liquid interface, here realized by setting $\alpha(0), \beta(0) = 0$. Under these conditions, only the effect of the diffuse-layer polarization can be observed, the fundamental polarization of the perfect conductor. As discussed in more detail in Bücker et al. (2018), normal electro-migration currents around the poles of the particle charge the electrolyte next to the particle surface until they are balanced by opposed diffusion currents driven by the resulting concentration gradients. At sufficiently small frequencies or after sufficiently long times, the total charge stored in the diffuse layer and mirrored on the particle is by a factor $a\kappa$ (where $\kappa = 1/\lambda_D$) larger than the quasi-instantaneously induced surface charge Σ_∞ (Bücker et al., 2018). The perturbation concentrations in the diffuse layer decay approximately exponentially with the distance from the surface, i.e., $\propto \exp[-\kappa(r-a)]$ (Wong, 1979; Bücker et al., 2018). The inner dashed lines in Figures 2 to 4 mark the distance at which the perturbations decay to $1/e$ of their respective values at the particle surface indicating the spatial extension of the field-induced diffuse layers.

From the third row of Figure 2 and the dashed grey curves in Figures 3 and 4 it is evident that the situation changes if a fixed surface potential of $\zeta = -50$ mV is considered: Here, we observe a significant reduction of the anion perturbation concentrations within the diffuse layer (first panel), while the resulting lack of charge is compensated by an amplification of the cation perturbation concentrations in the diffuse layer (second and third panel, better recognizable from the radial sections in Figures 3 and 4). Beyond the diffuse

layer covering the sub-micron particle (Figures 2 and 3), all ion concentrations increase (or respectively decrease) uniformly on the two opposite sides of the particle resulting in an electrically neutral salinity gradient around the particle. The development of this relatively long-range concentration gradient can be understood as a direct consequence of the unequal contributions of anions and cations to the conductivity of the static diffuse layer. Tangentially to the surface, electro-migration currents transport much more cations than anions, which in Figure 2 depletes cations to the left of the particle and accumulates them to the right. At the same time, more anions arrive at (are pulled away from) the right (left) side of the particle than can be transported through the diffuse layer, which explains the net electro-neutrality of the perturbation. The concentrations increase until the resulting opposite diffusion currents can balance the effect of the electro-migration currents, leading to the quasi-equilibrium situation seen in Figure 2. The process described in this paragraph is a volume-diffusion mechanism, which is similar to but should not be confused with the one arising from the reaction currents discussed in the next paragraph. Obviously, this mechanism is much weaker around the larger particle (Figure 4), where the presence of a static diffuse layer does not result in recognizable changes of the ion concentration in the zone marked as volume-diffusion layer.

The fourth row of Figure 2 and the black solid curves in Figures 3 and 4 show the influence of non-zero reaction currents, i.e., $\alpha, \beta > 0$, on the perturbations around an uncharged particle, i.e., $\zeta = 0$ mV. Here, not the unequal population of the static diffuse layer with anions and cations but the exclusive release and absorption of active cations at the surface causes an imbalance of electro-migration fluxes between the electrolyte far away and in the vicinity of the particle. As discussed in more detail previously (Bücker et al., 2018), the result is a coupling of the diffuse-layer polarization and the volume-diffusion process.

While the perturbations caused by the volume-diffusion process around charged particles (previous paragraph) appear clearly and have the same sign in all three ion concentrations; the reaction currents mainly affect the concentration of the active ions (see δn_3) and electroneutrality in the volume-diffusion region is ensured by a small reduction of δn_2 and a small increase of δn_1. The radial profiles in Figures 3 and 4 illustrate these distinct effects clearly.

The radial profiles in Figure 4 also show a second important difference between the concentration gradients due to the two different volume-diffusion mechanisms, which cannot be distinguished around the small particle: Only the reaction currents produce the plateaus observed in the region marked as volume-diffusion layer (black lines and symbols), which together with the decay at larger distances represent the $1/r^2$-dependence of the corresponding perturbation concentrations. The absence of these plateaus in the perturbation concentrations related to the asymmetric transport in the static diffuse layer (grey lines and symbols in Figure 4) indicates a much faster – probably exponential – decay with the distance from the particle surface and thus a much smaller thickness of the volume affected by the concentration gradient.

The last row of Figure 2 and the dashed black curves in Figures 3 and 4 show the coupling of all three polarization processes. From a direct comparison among the different maps and profiles, it can be seen that in this case, (1) the perturbation concentrations within the diffuse layer around small and large particles are largely controlled by the static diffuse layer, (2) those in the volume-diffusion region around the large particle only by the reaction current through the particle surface, and (3) those in the volume-diffusion region around the small particle by the reaction current through the particle surface and the static diffuse layer.

.

While effects of and interactions between the different polarization mechanisms are clearly reflected in the perturbation concentrations around the sub-micron particle, the resulting electric perturbation potentials (last column in Figure 2) hardly show any noticeable variation. The radial profiles of the perturbation potentials presented in Figure 5 show also only subtle differences. In both cases, the perturbation potential primarily shows the steep exponential decrease due to the space charge stored in the diffuse layer followed by a plateau due to the $1/r^2$ decay of the effective dipole moment of the particle. If no reaction currents are considered, i.e., for $\alpha, \beta = 0$, the charges of the diffuse layer fully screen the electric field. In this case, the potential profile outside the diffuse layer is equal to the one around a perfectly insulating sphere, the reflection coefficient of which can be obtained as $f = -1/2$ from potential theory[1]. Reaction currents through the interface (i.e., $\alpha, \beta > 0$) leak charges from the diffuse layer into the particle (and vice versa), which reduces the effective dipole moment of the particle and thus the perturbation potential along the plateau in Figure 5. The almost identical variations of the potential around charged (open symbols) and uncharged (filled symbols) particles suggest that the static diffuse layer has hardly any effect on the macroscopic response of the particle.

As mentioned in the previous section, Figures 3 to 5 show a good agreement of numerical (solid lines) and analytical (filled circles) results for the case of the uncharged particle, i.e., $\zeta = 0$ mV. The full analytical solution for all four perturbation quantities can be looked up in Bücker et al. (2018). Slight deviations between numerical and analytical solutions only become visible very close to the particle surface. As an explanation, we recall that the

[1]The reflection coefficient f of a sphere with conductivity σ_s embedded in a medium with homogeneous conductivity σ_m is $(\sigma_s - \sigma_m)/(\sigma_s + 2\sigma_m)$ (e.g. Maxwell, 1891).

smallest radial element size of our finite-element mesh is $\lambda_D/2$, which is a factor of 50 larger than the smallest radial distance displayed in the radial profiles in Figures 3 to 5. Thus the observed misfit does not indicate a systematic error but could be reduced by increasing the resolution of the mesh.

Spectral response

Figure 6 displays the effective conductivity spectra obtained for the sub-micron particle, i.e., $a = 0.1$ μm, in terms of the respective real ($\sigma'(\omega)$) and imaginary ($\sigma''(\omega)$) parts. The diffuse-layer relaxation, which dominates around such small particles, leads to a steep transition between the low and high-frequency limits of σ' and a narrow peak in the σ'' spectra. The small overshots of σ' at the angular frequency $1/\tau_{\mathrm{el}} = \sigma_0/(\varepsilon_0\varepsilon_r) \approx 10^{-7}$ rad/s can be attributed to the relaxation of the electrolyte solution (Bücker et al., 2018) and obey the Kramers-Kronig relations with the corresponding imaginary spectra (not shown here for brevity). The effect of a non-zero ζ-potential on the spectra in Figure 6 can be summarized under the following three main changes: The presence of a static diffuse layer (1) increases the direct-current limit of σ' (subsequently denominated by σ_{DC}), (2) reduces the maximum of σ'' (subsequently σ''_{max}), and (3) shifts the characteristic angular frequency, at which σ''_{max} is encountered, towards lower frequencies (subsequently ω_c).

Figure 7 shows that the effect of a non-zero ζ-potential on the spectral response of the large particle with $a = 10$ mm is different. For vanishing reaction currents, i.e., $\alpha(0), \beta(0) = 0$, we still observe the steep transition of σ' and the narrow peak of σ'' related to the diffuse-layer polarization. However, here σ_{DC} and σ''_{max} remain unaffected by the static diffuse layer and only the shift of ω_c to lower frequencies can be observed. If non-zero reaction currents

through the surface of the large particle are taken into account, i.e., for $\alpha(0), \beta(0) > 0$, the volume-diffusion process becomes dominant resulting in a broadening of the transition region, a broadening and reduction of the σ''-peak, and a substential reduction of the characteristic angular frequency ω_c. In this regime no effect of the static diffuse layer on the spectral response can be detected.

In the following, we will study the dependency of the three spectral parameters σ_{DC}, σ''_{max}, and ω_c on the ζ-potential in more detail and provide some possible explanations for the observed changes.

The left panel of Figure 8 shows the variation of σ_{DC} with the ζ-potential for two different particle radii ($a = 0.1$ and 31.6 μm). As we know, an increasing magnitude of the (negative) ζ-potential results in an increase of cation and a decrease of anion concentrations in the static diffuse layer. Because the increase of the cation concentrations with ζ is much larger than the decrease of the anion concentration, the surface conductivity increases with the magnitude of the ζ-potential, which results in the increase of σ_{DC} observed in Figure 8. As the total volume fraction occupied by the static diffuse layer of fixed thickness λ_D decreases with increasing particle size, the increase of σ_{DC} with ζ is most pronounced around the smaller particle (0.1 μm) and becomes almost negligible around the larger (31.6 μm) particle.

Above we saw that – provided that no reaction currents are allowed to cross the surface – a fully developed induced diffuse layer lets the perfectly conducting particle effectively (i.e., outside the diffuse layer) behave like a non-conducting particle (see Figure 5). At the same time, the static diffuse layer partly compensates the effect of the induced diffuse layer and slightly increases the effective conductivity. In order to understand the contribution of the

static diffuse layer, we can try to describe the variation of σ_{DC} with ζ by the corresponding expressions known from the classical theory for non-conducting particles. According to O'Konski (1960), the effect of the surface conductivity K can be taken into account by adding the conductivity $2K/a$ to the conductivity of the particle. If the particle is non-conducting, which in our case is true in the low-frequency limit and outside the induced diffuse layer, the effective conductivity of the particle is given by

$$\sigma_p = \frac{2K}{a}. \tag{23}$$

As our model does not include a Stern layer, K only considers the conductivity increment due to the static diffuse layer. For a thin static diffuse layer, i.e., $a\kappa \gg 1$, the surface conductivity K can be approximated using Bikerman's formula (e.g. Shilov et al., 2001). Because we do not consider electro-osmotic coupling, we evaluate this formula in the high-viscosity limit, where

$$K \approx 2\sigma_0 \lambda_D \left[\cosh\left(\frac{e\zeta}{2kT}\right) - 1\right]. \tag{24}$$

The effective DC conductivity of a particle with conductivity σ_p immersed in a medium of conductivity σ_0 can be obtained from inserting the effective reflection or dipole coefficient (e.g. from Shilov et al., 2001)

$$f_{\mathrm{DC}} = \frac{\sigma_p - \sigma_0}{\sigma_p + 2\sigma_0}, \tag{25}$$

into the Maxwell-Garnett mixing rule, equation 21. The predicted variation of σ_{DC} with ζ is illustrated in the left panel of Figure 8 (solid lines) along with the corresponding numerical results (black open symbols).

Particularly for the smaller particle, this analytical approximation overestimates the conductivity increment produced by the static diffuse layer. There are various reasons for the observed deviation: Equations 23 through 25 are only valid in the thin double layer limit, i.e.,

$a \gg \lambda_D$. Furthermore, the Bikerman model of surface conductivity does not consider the volume-diffusion polarization of the static diffuse layer observed in our simulation results, which is expected to reduce the effective conductivity increment, nor the coupling with the induced diffuse layer. Despite these shortcomings, the qualitative agreement with the modelled response is relatively good and provides an additional plausibility check of our numerical implementation.

Note that the comparison with the response of a non-conducting particle is only sensible in the low-frequency limit, where the perfectly conducting particle behaves like an insulator. At higher frequencies, the different natures of the particles lead to fundamentally different frequency dependencies of the effective conductivity (see the Discussion section for more detail).

The right panel of Figure 8 shows the variation of $\sigma''_{\max}$ (i.e., the value of σ'' at the characteristic frequency of each individual spectral response), which is often taken as a measure of the magnitude of the polarization. If no reaction currents are considered (grey diamonds), $\sigma''_{\max}$ decreases with the magnitude of ζ. This decrease is most pronounced for the smallest particle, i.e., $a = 0.1$ μm, and hardly noticeable for the largest, i.e., $a = 10$ mm. For the smallest particle, the variation of $\sigma''_{\max}$ with ζ does almost not change when reaction currents are added to the model (black circles). All responses discussed so far are dominated by the relaxation of the diffuse layer, such that we can conclude that the magnitude of this polarization process generally decreases with increasing diffuse charge density at the particle surface. The opposite is the case when the volume-diffusion process becomes dominant, $\sigma''_{\max}$ increases with the magnitude of ζ. We observe this around the intermediate particle, i.e., $a = 31.6$ μm, if reaction currents are considered. Also in the case of non-zero reaction currents, the effect of ζ becomes almost imperceptible around the

largest particle, i.e., $a = 10$ mm.

Relaxation time

Due to its strong dependence on geometrical parameters, the relaxation time τ, here defined as the inverse of the characteristic angular frequency ω_c, is often used as a proxy for the size of the conducting particles. Hence, a good understanding of the effect of the ζ-potential on this important spectral parameter would be desirable. Figure 9 illustrates the variation of τ with the particle radius a for different surface characteristics. The response of uncharged particles shows the typical division into two regimes (e.g. Bücker et al., 2018): The $\tau \propto \lambda_D a$ increase can be attributed to the diffuse-layer relaxation, while the much steeper $\tau \propto a^2$ variation is related to the volume-diffusion mechanism, which dominates around larger particles if reaction currents through the particle surface are taken into account. This division into two regimes is also valid for charged particles, i.e., $\zeta = -50$ mV. The only effect of the static diffuse layer around the particles is a slight increase of of the relaxation times of the diffuse layer ($\propto \lambda_D a$) for radii $a \gtrsim 1$ μm. The relaxation times of the volume-diffusion polarization ($\propto a^2$), in contrast, remain practically unaffected.

Figure 10, which illustrates the variation of the relaxation times with the ζ-potential for three differently sized particles, confirms this general observation. We also see that the variation of the relaxation time of the diffuse layer, i.e., $\alpha(0), \beta(0) = 0$, with ζ is relatively flat around 0 mV, becomes steepest around ± 25 to ± 75 mV and then again flattens out towards higher magnitudes of ζ. This behavior is symmetric with respect to $\zeta = 0$ mV and thus not affected by the sign of the diffuse surface charge. In contrast, the practically constant relaxation time of the volume-diffusion mechanism (black lines and symbols in

Figure 10) presents a slightly asymmetric behaviour, which becomes most noticeable at large magnitudes of the ζ-potential.

At first glance, the increase of the relaxation time of the diffuse layer with ζ seems counter-intuitive: The static diffuse layer increases the conductivity in the vicinity of the particle as described by the surface conductivity K. At the same time, the relaxation time is proportional to the Debye length and thus to the square root of the inverse of the conductivity of the electrolyte around the particle, i.e., $\tau \propto 1/\sqrt{\sigma_0}$ (e.g. from Bücker et al., 2018), which would rather imply a decrease of τ with ζ. However, the concentration polarization produced by the unequal anion and cation fluxes through the static diffuse layer rather seems to delay charging and relaxation of the induced diffuse layers related to the observed increase of τ with ζ.

The relative insensitivity of the relaxation time of the volume-diffusion process (the one produced by the reaction currents) to changes in ζ is in accordance to the fact that the corresponding volume-diffusion layer is practically unaffected by the presence of the static diffuse layer (see e.g. Figure 4). Obviously, this process does not respond to changes in the (surface) conductivity, which is plausible for a purely diffusion-controlled mechanism.

DISCUSSION

Perfectly conducting vs. non-conducting particles

Treatments of the low-frequency polarization response of charged (non-conducting) dielectric particles can be roughly classified into two groups; models of the first group stress the polarization response of the Stern or Helmholtz layer of counter-ions tightly bound to the particle surface (e.g. Schwarz, 1962; Schurr, 1964; Leroy et al., 2008). Under the influence

of an external electric field, these charges rearrange along the surface but cannot leave (or enter) the Stern layer. The maximum polarization is assumed to be controlled by an equilibrium between tangential electro-migration and diffusion currents resulting in the typical relaxation time scale of the Stern layer $\tau = a^2/(2D)$. The influence of the outer diffuse layer is only considered in terms of the real-valued conductivity increment $2K/a$ proposed by O'Konski (1960), which does not actively contribute to the polarization. Models of the second group, in contrast, only study the polarization response of the diffuse layer. While most treatments neglect the polarization response of the Stern layer (e.g. Chew and Sen, 1982a; DeLacey and White, 1981), there are also approaches attempting to incorporate its effect (e.g. Shilov et al., 2001). The polarization of the static diffuse layer arises due to the unequal cation and anion transport by electro-migration currents along the surface and usually also relaxes on a time scale $\tau \propto a^2/D$. In absence of a fixed diffuse surface charge and thus for a vanishing ζ-potential, the models of both groups do not predict any polarization response, except for the Maxwell-Wagner polarization at high frequencies (i.e., $\approx 1/\tau_{\mathrm{el}}$).

In comparison to these polarization mechanisms around non-conducting particles, the case of perfectly conducting particles is fundamentally different. Here, the main mechanism responsible for the large low-frequency dispersion of the effective conductivity of the suspension is the dynamic charging of the field-induced (and not the static) diffuse layer, which is a direct consequence of the high conductivity contrast between particle and electrolyte. In contrast to both mechanisms observed for non-conducting particles, the pure polarization of the field-induced diffuse layer relaxes on a time scale $\tau = \lambda_D a/(2D)$. Only if reaction currents, which have not been addressed in the theories for non-conducting particles, are taken into account the coupling with the resulting volume-diffusion mechanism yields a

relaxation time $\tau \propto a^2$.

The present numerical study indicates that the effect of ζ-potential and static diffuse layer should be considered of secondary importance for the effective conductivity of suspensions of perfectly conducting particles – at least for typical parameter values. Interestingly, the corresponding surface conductivity rather decreases the polarization magnitude, i.e., $\sigma''_{\max}$, and thus its effect is exactly opposite to the one it has in the case of non-conducting particles.

In the case of non-conducting particles, the Stern layer usually plays an even more important role for the observed polarization phenomena (e.g. Schwarz, 1962; Schurr, 1964; Leroy et al., 2008) than the diffuse layer. However, our model does not include any polarization effect due to the Stern layer. We justify this simplification based on the assumed infinite conductivity of the particle, which results in a vanishing tangential electric field along the particle surface (and at small distances from the surface). This is due to an immediate redistribution of charges, which cancels out any electric field within the particle volume and along its surface. Thus, tangential electromigration currents within a thin Stern layer, which cause a large polarization around non-conducting particles, should either be zero or very small.

In summary, the role of surface conductivity around perfectly conducting particles is completely different to the one it plays for the polarization of non-conducting particles. Therefore, the polarization of the static diffuse layer around perfectly conducting particles should by no means be confused with the main polarization mechanisms due to the dynamic charging of the diffuse layer and the volume-diffusion process driven by reaction currents.

Potential for nano-particle characterization

To date only few studies have investigated the particular IP response of metallic nano-particles (Joyce et al., 2012; Shi et al., 2015; Aal et al., 2017), but the obtained results encourage further research to advance this exciting new application. The strong response of metallic particles and the well-known fact that the polarization magnitude scales with the volumetric metal content (e.g. Wong, 1979; Misra et al., 2017) make it a suitable method to monitor nano-particle injection experiments (Flores Orozco et al., 2015). Besides the mere localization and quantification, some researchers have even suggested that IP measurements could aid in the characterization of the in-situ chemical condition and reactivity of the particle surfaces (e.g. Shi et al., 2015). The strong correlation between the ζ-potential (i.e., the fixed diffuse surface charge) on both surface reactivity (e.g. Sund et al., 2011) and IP response of non-conducting particles (e.g. Leroy et al., 2008) justified this hope.

Generally speaking, our modelling results also indicate that the sheer size of nano-particles favours such applications of the IP method: From Figure 8 we see that the smaller the particle is, the more sensitive both σ_{DC} and σ''_{max} become with respect to variations of the ζ-potential. For the 0.1 μm particle, the maximum relative changes of both spectral parameters are approximately 15% over the studied range of ζ-potentials from 0 to -125 mV. These variations are small but detectable. With increasing particle size, the sensitivity of both parameters to changes in ζ decreases rapidly. Already for micro-scale particles, here 31.6 μm, they are expected to be almost insensitive – except for σ''_{max} in the case of non-zero reaction currents.

The situation is very different with regard to the sensitivity of the relaxation time to variations of the ζ-potential. Figures 9 and 10 show that here, in contrast to σ_{DC} and σ''_{max}, a

significant increase of the relaxation time can only be observed for micro-particles or larger, i.e., $a \gtrsim 1$ μm, and in absence of reaction currents. Under these conditions, the relaxation time of the pure diffuse-layer polarization increases by a factor 5 from 0 mV to $\pm$125 mV, with the highest sensitivity in the range between $\pm$25 through $\pm$75 mV. As the same two Figures show the relaxation time of the volume-diffusion process, which dominates for larger particles sizes and non-zero reaction currents, is expected to be practically insensitive to changes of the ζ-potential. However, in this regime the relaxation time is highly sensitive to the reaction current through the particle surface, which in turn is a direct measure for the reactivity of the particle surface. This effect can be of interest to monitor particle-injection experiments, where particle-surface properties change over time (e.g., engineered particle coatings, Flores Orozco et al., 2015)), or conditions with varying availability of active ionic species, e.g. due to biogeochemical processes (e.g., Flores Orozco et al., 2011).

Despite of the theoretical potential of the IP method to characterize surface properties such as ζ-potential and reactivity, the high characteristic frequencies of the relaxation processes around nano-particles impose a practical limit: Typical laboratory set-ups only permit to determine the complex conductivity response of material samples up to frequencies of 1 to 40 kHz, and can therefore only resolve the increasing flank of the relaxation peak (e.g. Aal et al., 2017). In this case, the determination of the characteristic frequency might become too imprecise to detect the small variations of τ with ζ. Other researchers, in contrast, were able to observe the relaxation peak of sub-micron silver and zero-valent iron particles at sufficiently low frequencies (Joyce et al., 2012). In field experiments with array lengths in the meter to dekameter range, electromagnetic induction usually masks the IP response at frequencies $> 10 - 100$ Hz (e.g. Flores Orozco et al., 2011, 2012), which further reduces the detectability of nano-particles in larger-scale applications.

Limitations of the model

In part 1 of this series (Bücker et al., 2018), we discussed the limitations inherent to the model by Wong (1979) including our own extensions. Obviously, the numerical model presented in this second part suffers from the same set of shortcomings inherited from the base model. To mention some of the remaining issues, (1) it ignores the fact that most metal-bearing minerals are rather semiconductors than metallic conductors , (2) it does not consider dynamic charging of the Stern layer (e.g. Merriam, 2007), (3) it neglects particle-particle interactions between adjacent grains, which is inherent to the mixing rule used for the up-scaling, (4) it does not treat effects of non-spherical geometries or surface roughness, and (5) having even more model parameters, its application to real data is expected to be even more tedious (e.g. Placencia-Gómez and Slater, 2014).

In the light of recently developed semiconductor-polarization models (e.g., Revil et al., 2015b; Misra et al., 2016a,b; Abdulsamad et al., 2017), it is worth reconsidering the assumption of an infinite conductivity of the metallic particle. In his analysis, Wong (1979) argued that if "the conductivity [...] of the mineral is a hundred or a thousand times the conductivity [...] of the surrounding medium" (i.e. the electrolyte), the particle could be considered a perfect conductor. However, this argumentation only assesses the (direct-current) conductivity of the involved materials, which is not sufficient in the context of a frequency-dependent model.

The situation described by the zero-potential boundary condition (15) requires the charges on the particle to relax much faster than the variation of the external excitation. In metallic conductors, the charge relaxation time can be roughly approximated by twice the collision time of the free electrons (e.g., Ashby, 1975). At room temperature, typical

collision times in elemental metals are in the order of 10^{-15} s to 10^{-14} s, such that the characteristic frequency of charge relaxation is well beyond the relevant frequency range and the assumption of a perfect conductor remains justified. The analysis by Revil et al. (2015b) and Revil et al. (2015a) suggests that the situation changes fundamentally if semiconducting minerals, such as pyrite or magnetite, are considered. Here, the diffusion-controlled relaxation of the charge carriers insight the semiconducting particle not only leads to a much slower response of the solid particle but seems to be the main polarization mechanism in the typical IP frequency range. With this in mind, the application of the present polarization model (as well as any model that rests on the assumption of a perfectly conductive solid phase) should clearly be limited to the case of metallic conductors.

In addition to the known limitations (1) through (5), the assumption of a constant ζ-potential used in this study might also be unrealistic. In particular, the large field-induced variations of the ion concentrations close to the particle surface rise doubts whether the constant-ζ-potential boundary condition, i.e., equation 15, can be adequate. This limitation is also inherited from the Wong model, which – from our new perspective – simply describes the special case of $\zeta = 0$, i.e., at the point of zero charge of the metal surface. Determining the ζ-potential self-consistently from a speciation model for the particle-electrolyte interface might result in a more realistic boundary condition, which can account for the complex mutual dependency between the diffuse layer and the surface (including the Stern layer).

CONCLUSION

We have developed a numerical approach to study the effect of a static diffuse layer on the electro-chemical polarization of a perfectly conducting particle. In comparison to the response of a particle without such a static diffuse layer, the observed changes are relatively

small, which implies that the effect of surface conductivity is of secondary importance for the polarization of perfectly conducting or metallic particles. In particular around relatively large particles (compared to the Debye length), the diffuse surface charge on the particle is practically not expected to influence the macroscopic response at all.

For nano- and small micro-scale particles, however, the three important spectral parameters – the low-frequency limit of the effective conductivity σ_{DC}, the polarization magnitude σ''_{max}, and the relaxation time τ – do reveal measurable responses to variations of the ζ-potential (or the constant diffuse surface charge). Therefore, our findings are of particular interest for the interpretation of IP experiments designed to find a link between complex conductivity response and chemical surface conditions of metallic nano- and micro-scale particles.

The present study advances the basic understanding of the polarization mechanism around perfectly conducting particles, quantifies the previously completely disregarded effect of diffuse surface charge on the polarization response, and opens the possibility for an application of the IP method for the improved characterization of the chemical state of metallic nano- and microscale particles.

APPENDIX A

ADAPTATION OF THE EXCHANGE CURRENT

Our description of the exchange current strictly adheres to the one proposed by Wong (1979). However, while Wong can assume the bulk concentration of the active cations n_3^{∞} at the particle surface, according to equation 7, the equilibrium concentration at a charged surface is given by $n_3^{(0)}(\zeta) = n_3^{\infty} \exp\left[-e\zeta/(kT)\right]$, which requires some adaptions of the

known expressions.

The fundamental metal deposition-dissolution reaction

$$\mathrm{M}^{+} + \mathrm{e}^{-} \leftrightarrows \mathrm{M}_{(\mathrm{ads})} \tag{A-1}$$

remains unchanged. Here, M^{+} denotes the metal cation in solution, e^{-} an electron and $\mathrm{M}_{(\mathrm{ads})}$ a metal atom adsorbed to the particle surface. The net exchange current density due to the above reaction writes [equation (23) in Wong (1979)]

$$i = k_{-}[\mathrm{M}_{(\mathrm{ads})}]e \exp\left[e\eta/(2kT)\right] - k_{+}[\mathrm{M}^{+}]e \exp\left[-e\eta/(2kT)\right], \tag{A-2}$$

where we have already assumed a symmetry factor of 1/2. The parameters k_{+} and k_{-} are rate constants, $[\mathrm{M}_{(\mathrm{ads})}]$ and $[\mathrm{M}^{+}]$ are concentrations of active cations and adsorbed atoms (in ions/m^3), and η is the current-producing overpotential.

Under undisturbed conditions, i.e., without any external excitation, the overpotential η is zero by definition and the modified concentration of active cations at the particle surface is given by $n_3^{(0)}(\zeta)$, which includes the cation excess in the static diffuse layer caused by the non-vanishing surface potential ζ. Wong's expression for the equilibrium exchange current, his equation (24), therefore becomes

$$i_0 = k_{-}[\mathrm{M}_{(\mathrm{ads})}]e = k_{+}n_3^{(0)}(\zeta)N_A e, \tag{A-3}$$

where N_A is Avogadro's constant ($6.0221 \cdot 10^{23}$ mol^{-1}).

As Wong (1979) discusses in more detail, for small overpotentials $\eta \ll e/(2kT)$) the non-equilibrium exchange current due to a non-zero overpotential can be linearized resulting in

$$i \approx i_0 e\eta/(kT) \quad \text{or} \quad i \approx i_0 e/(kT)\mathbf{E}\cdot\mathbf{n}\; l, \tag{A-4}$$

where $\mathbf{E} \cdot \mathbf{n}$ is the component of the electrical field normal to the particle surface ($\mathbf{n}$ is the unit normal vector pointing into the electrolyte) and l is the characteristic distance of closest approach by the active cations to the surface.

Even in absence of a current-producing overpotential, a perturbation $\delta n_3(\zeta)$ of the active cation concentration from the equilibrium value $n_3^{(0)}(\zeta)$ can generate the net exchange current

$$\begin{aligned} i &= k_-[\mathrm{M}_{(\mathrm{ads})}]e - k_+[n_3^{(0)}(\zeta) + \delta n_3(\zeta)]N_A e \\ &= i_0 - i_0 - k_+ \delta n_3(\zeta) N_A e \\ &= -k_+ \delta n_3(\zeta) N_A e. \end{aligned} \tag{A-5}$$

Note that the net current density due to a positive $\delta n_3(\zeta)$ is negative (toward the center of the particle).

The total exchange current density is then obtained as the sum of the one caused by a non-zero overpotential and a perturbation of the active cation concentration from the equilibrium and writes

$$i \approx \alpha(\zeta) n_3^{(0)}(\zeta) N_A e \mathbf{E} \cdot \mathbf{n} - \beta(\zeta) \delta n_3(\zeta) N_A e, \tag{A-6}$$

where $\alpha(\zeta) = i_0 l/(n_3^{(0)}(\zeta) N_A kT)$ and $\beta = k_+ = i_0/(n_3^{(0)}(\zeta) N_A e)$ are functions of the ζ-potential. Wong (1979) estimates his values of $\alpha(0) = i_0 l/(n_3^{\infty} N_A kT)$ and $\beta(0) = i_0/(e n_3^{\infty} N_A)$ from experimentally determined values of the equilibrium reaction current density i_0. If we use the same experimental values as starting point and assume that the particles used also had a non-vanishing static surface potential, we find $\alpha(\zeta) = \alpha(0) \exp[e\zeta/(kT)]$ and $\beta(\zeta) = \beta(0) \exp[e\zeta/(kT)]$ (by comparison with the expressions by Wong). Note that Equation A-6 defines an electrical current density in A/m^2, i.e. the corresponding current densities in mol/(m^{2}s) as needed for the corresponding boundary condition, equation 17,

can be obtained by dividing i by $F = N_A e$.

APPENDIX B

IMPLEMENTATION INTO THE COMSOL COEFFICIENT FORM PDE

The COMSOL partial differential equation (PDE) interface in coefficient form allows the specification of PDEs and systems of PDEs of the general type

$$e_a \frac{\partial^2 u}{\partial t^2} + d_a \frac{\partial u}{\partial t} + \nabla \cdot (-c\nabla u - \alpha u + \gamma) + \beta \cdot \nabla u + au = f \tag{B-1}$$

with general boundary conditions

$$-\mathbf{n} \cdot (-c\nabla u - \alpha u + \gamma) = g - qu \quad \text{and} \tag{B-2}$$

$$u = s, \tag{B-3}$$

where u denotes the dependent variable and $\mathbf{n}$ is the inward-pointing unit normal vector (i.e., into the electrolyte) on the respective boundary. Note that actually COMSOL defines the normal vector reversely (outward-pointing) and consequently it appears with reversed sign in equation B-2. The coefficients e_a, d_a, c, α, γ, β, a, f, q, g, and s are used to describe the specific problem to be modelled. Equation B-2 is a generalized Neumann boundary condition and equation B-3 a Dirichlet boundary condition.

Static solution

With these definitions, the numerical implementation of the static problem from equations 7 and 8 with boundary conditions 9 and 10 is straightforward. If we define the dependent

variable $u_1 = U^{(0)}(\mathbf{r})$, the PDE coefficients must be

$$c = 1 \quad \text{and} \tag{B-4}$$

$$f = \frac{F}{\varepsilon_0 \varepsilon_r} \sum_{j=1}^{3} z_j n_j^\infty \exp\left(-\frac{z_j e}{kT} u\right). \tag{B-5}$$

Note that throughout this step-by-step instruction we will use the convention that all coefficients that are not mentioned specifically are assumed to be zero. Assuming mono-valent ions $|z_j| = 1$ and making use of the electro-neutrality condition in the bulk electrolyte $n_1^\infty = n_2^\infty + n_3^\infty$, the coefficient f can be simplified to

$$f = -\frac{2 n_1^\infty F}{\varepsilon_0 \varepsilon_r} \sinh\left(\frac{e}{kT} u\right). \tag{B-6}$$

On the top boundary (at $y = L$), on the left ($x = -L$), and on the right ($x = L$) boundary, we define

$$s = 0, \tag{B-7}$$

while on for the metal surface (at $x^2 + y^2 = a^2$ for the spherical particle) we set

$$s = \zeta \tag{B-8}$$

to implement the Dirichlet boundary conditions 10 and 9, respectively. Defining the axis $y = 0$ as symmetry axis (selecting rotational symmetry in the model setup), no specific boundary conditions must be defined on this boundary.

Frequency-dependent solution

For the solution of the frequency-dependent case, we need to implement the system of four coupled PDEs described in equations 11 and 12. In the system case, the dependent variable

u in equation B-1 becomes a column vector of length 4. We define

$$\mathbf{u}_2 = \begin{bmatrix} u_{21} \\ u_{22} \\ u_{23} \\ u_{24} \end{bmatrix} = \begin{bmatrix} \delta n_1(\mathbf{r},\omega) \\ \delta n_2(\mathbf{r},\omega) \\ \delta n_3(\mathbf{r},\omega) \\ \delta U(\mathbf{r},\omega) \end{bmatrix}. \tag{B-9}$$

Assuming isotropy of all of its elements, the coefficient c becomes a 4-by4 coefficient matrix.

In our case, $\underline{c}$ writes

$$\underline{c} = \begin{bmatrix} D & 0 & 0 & -\mu_1 n_1^{\infty} \exp(\frac{e}{kT} u_1) \\ 0 & D & 0 & \mu_2 n_2^{\infty} \exp(-\frac{e}{kT} u_1) \\ 0 & 0 & D & \mu_3 n_3^{\infty} \exp(-\frac{e}{kT} u_1) \\ 0 & 0 & 0 & 1 \end{bmatrix}, \tag{B-10}$$

where u_1 denotes the scalar static solution (for the electrical potential only). The coefficient matrices

$$\underline{\alpha} = \begin{bmatrix} -\mu_1 \nabla u_1 & 0 & 0 & 0 \\ 0 & \mu_2 \nabla u_1 & 0 & 0 \\ 0 & 0 & \mu_3 \nabla u_1 & 0 \\ 0 & 0 & 0 & 0 \end{bmatrix}, \tag{B-11}$$

and

$$\underline{a} = \begin{bmatrix} i\omega & 0 & 0 & 0 \\ 0 & i\omega & 0 & 0 \\ 0 & 0 & i\omega & 0 \\ \frac{F}{\varepsilon_0 \varepsilon_r} & -\frac{F}{\varepsilon_0 \varepsilon_r} & -\frac{F}{\varepsilon_0 \varepsilon_r} & 0 \end{bmatrix} \tag{B-12}$$

complete the description of our system of PDEs in coefficient form. Note that each element $\alpha_{i,j} = [\alpha_{i,j,1}, \alpha_{i,j,2}]^T$ is a two-element column vector where the third indices correspond to the spatial coordinates x and y.

As mentioned in the main text, because of the cylindrical symmetry, the solution of the system of PDEs can be carried out on a two-dimensional modelling domain with coordinates x and y (see Figure 1). Thus, the position vector and the gradient operator become

$$\mathbf{r} = \begin{bmatrix} x \\ \\ y \end{bmatrix} \text{ and } \nabla = \begin{bmatrix} \partial_x \\ \\ \partial_y \end{bmatrix}, \tag{B-13}$$

respectively. Although we are actually interested in solving the system of PDEs in cylindrical coordinates, we will first proceed with the formulation of the system in the two Cartesian coordinates x and y and further below provide a simple conversion to cylindrical coordinates.

The problem description for the numerical modelling is completed by the following boundary conditions. Far from the particle surface (i.e., for $r \to \infty$), we requested the perturbation potential to approximate the exciting potential $-\mathbf{E} \cdot \mathbf{r}$ and the perturbation ion concentrations to vanish. Therefore, on the **left and right boundary**, we define Dirichlet boundary conditions by setting

$$\mathbf{s} = \begin{bmatrix} 0 \\ \\ 0 \\ \\ 0 \\ \\ E_0 L \end{bmatrix} \quad \text{and} \quad \mathbf{s} = \begin{bmatrix} 0 \\ \\ 0 \\ \\ 0 \\ \\ -E_0 L \end{bmatrix}, \tag{B-14}$$

respectively.

On the **top boundary**, we implement a zero-flux boundary condition for all four dependent variables. This results in vanishing normal fluxes for all three ionic species and a vanishing normal electrical field. Again, due to the rotational symmetry, no boundary conditions must be defined on the symmetry axis (i.e., along $y = 0$).

On the **particle surface**, we implement mixed boundary conditions consisting of one

Dirichlet condition for the electric potential, equation 15, and generalized Neumann conditions for the three ion fluxes, equations 16 through 17. To define the boundary conditions on the ion fluxes, we set

$$\underline{q} = \begin{bmatrix} 0 & 0 & 0 & 0 \\ 0 & 0 & 0 & 0 \\ 0 & 0 & \beta(\zeta) & 0 \\ 0 & 0 & 0 & 0 \end{bmatrix} \tag{B-15}$$

and

$$\mathbf{g} = \begin{bmatrix} 0 \\ 0 \\ \alpha(\zeta) n_3^{\infty} \exp\left(-\frac{e}{kT} u_1\right) \mathbf{n} \cdot \nabla u_{24} \\ 0 \end{bmatrix}, \tag{B-16}$$

where $\mathbf{n} \cdot \nabla u_{24} = n_x \partial_x u_{24} + n_y \partial_y u_{24}$. A Dirichlet boundary condition component is specified for the fourth component by setting

$$s = 0, \tag{B-17}$$

which overwrites the above no-flux boundary condition (only for the perturbation potential). The Dirichlet boundary condition for the first three components are deactivated and the generalized Neumann boundary conditions described by $\underline{q}$ and $\mathbf{g}$ remain valid for the first three components.

Conversion to cylindrical coordinates

As mentioned above, the software expects the equations to be defined in a Cartesian system with two space dimensions. That means, that if we assume isotropic media (i.e., $\underline{c}$ is a 4-by-4

matrix) the i-th equation of our system is given by

$$\sum_j \left[- \left(\partial_x c_{i,j} \partial_x + \partial_y c_{i,j} \partial_y \right) u_j - \left(\partial_x \alpha_{i,j,1} + \partial_y \alpha_{i,j,2} \right) u_j + a_{i,j} u_j \right] = 0, \tag{B-18}$$

where we have already dropped all vanishing coefficients (i.e., e_a, d_a, γ, etc.). However, we actually seek to solve a system in cylindrical coordinates, the i-th component of which should write

$$\sum_j \left[- \left(\frac{1}{r} \partial_r r c_{i,j} \partial_r + \partial_z c_{i,j} \partial_z \right) u_j - \left(\frac{1}{r} \partial_r r \alpha_{i,j,1} + \partial_z \alpha_{i,j,2} \right) u_j + a_{i,j} u_j \right] = 0 \tag{B-19}$$

instead. If we simply multiply the entire system by r, we get

$$\sum_j \left[- \left(\partial_r r c_{i,j,1,1} \partial_r + \partial_z r c_{i,j,2,2} \partial_z \right) u_j - \left(\partial_r r \alpha_{i,j,1} + \partial_z r \alpha_{i,j,2} \right) u_j + r a_{i,j} u_j \right] = 0, \tag{B-20}$$

which can be converted to the form supported by software. Defining r as y and z as x yields the modified system

$$\nabla \cdot \left(-y \underline{c} \nabla \mathbf{u} - y \underline{\alpha} \mathbf{u} \right) + y \underline{a} \mathbf{u} = 0 \tag{B-21}$$

Thus, it is sufficient to multiply the three coefficient matrices $\underline{c}$, $\underline{\alpha}$, and $\underline{a}$ by y to transform the problem to cylindrical coordinates. Note that the boundary coefficients $\underline{q}$ and $\mathbf{g}$ have to be multiplied by y, too, while $\mathbf{r}$ remains unchanged.

REFERENCES

Aal, G. A., E. A. Atekwana, and D. D. Werkema, 2017, Complex conductivity response to silver nanoparticles in partially saturated sand columns: Journal of Applied Geophysics, **137**, 73–81.

Abdulsamad, F., N. Florsch, and C. Camerlynck, 2017, Spectral induced polarization in a sandy medium containing semiconductor materials: experimental results and numerical modelling of the polarization mechanism: Near Surface Geophysics, **15**, 669–683.

Ashby, N., 1975, Relaxation of charge imbalances in conductors: American Journal of Physics, **43**, 553–555.

Atkins, P., and J. De Paula, 2013, Elements of physical chemistry: Oxford University Press, USA.

Bazant, M. Z., K. Thornton, and A. Ajdari, 2004, Diffuse-charge dynamics in electrochemical systems: Physical review E, **70**, 021506.

Boulangé-Petermann, L., A. Doren, B. Baroux, and M.-N. Bellon-Fontaine, 1995, Zeta potential measurements on passive metals: Journal of colloid and interface science, **171**, 179–186.

Bücker, M., A. Flores Orozco, and A. Kemna, 2018, Electro-chemical polarization around metallic particles – part 1: The role of diffuse-layer and volume-diffusion relaxation: Geophysics, **83**, E203–E217.

Chew, W., and P. Sen, 1982a, Dielectric enhancement due to electrochemical double layer: thin double layer approximation: The Journal of Chemical Physics, **77**, 4683–4693.

———, 1982b, Potential of a sphere in an ionic solution in thin double layer approximations: The Journal of Chemical Physics, **77**, 2042–2044.

DeLacey, E. H., and L. R. White, 1981, Dielectric response and conductivity of dilute

suspensions of colloidal particles: Journal of the Chemical Society, Faraday Transactions 2: Molecular and Chemical Physics, **77**, 2007–2039.

Flores Orozco, A., A. Kemna, C. Oberdörster, L. Zschornack, C. Leven, P. Dietrich, and H. Weiss, 2012, Delineation of subsurface hydrocarbon contamination at a former hydrogenation plant using spectral induced polarization imaging: Journal of contaminant hydrology, **136**, 131–144.

Flores Orozco, A., M. Velimirovic, T. Tosco, A. Kemna, H. Sapion, N. Klaas, R. Sethi, and L. Bastiaens, 2015, Monitoring the injection of microscale zerovalent iron particles for groundwater remediation by means of complex electrical conductivity imaging: Environmental science & technology, **49**, 5593–5600.

Flores Orozco, A., K. H. Williams, P. E. Long, S. S. Hubbard, and A. Kemna, 2011, Using complex resistivity imaging to infer biogeochemical processes associated with bioremediation of an uranium-contaminated aquifer: Journal of Geophysical Research: Biogeosciences, **116**.

Gurin, G., K. Titov, Y. Ilyin, and A. Tarasov, 2015, Induced polarization of disseminated electronically conductive minerals: a semi-empirical model: Geophysical Journal International, **200**, 1555–1565.

Joyce, R. A., D. R. Glaser, D. D. Werkema, and E. A. Atekwana, 2012, Spectral induced polarization response to nanoparticles in a saturated sand matrix: Journal of applied geophysics, **77**, 63–71.

Leroy, P., A. Revil, A. Kemna, P. Cosenza, and A. Ghorbani, 2008, Complex conductivity of water-saturated packs of glass beads: Journal of Colloid and Interface Science, **321**, 103–117.

Maxwell, J. C., 1891, A treatise on electricity and magnetism: Clarendon Press, Oxford.

Merriam, J., 2007, Induced polarization and surface electrochemistry: Geophysics, **72**, F157–F166.

Misra, S., C. Torres-Verdín, D. Homan, and J. Rasmus, 2017, Dispersive and directional electrical conductivity and dielectric permittivity of conductive-mineral-bearing samples derived from multifrequency tensor electromagnetic induction measurements: Geophysics, **82**, D211–D223.

Misra, S., C. Torres-Verdín, A. Revil, J. Rasmus, and D. Homan, 2016a, Interfacial polarization of disseminated conductive minerals in absence of redox-active speciespart 1: Mechanistic model and validation: Geophysics, **81**, E139–E157.

———, 2016b, Interfacial polarization of disseminated conductive minerals in absence of redox-active speciespart 2: Effective electrical conductivity and dielectric permittivity: Geophysics, **81**, E159–E176.

Nernst, W., 1888, Zur Kinetik der in Lösung befindlichen Körper: Zeitschrift für physikalische Chemie, **2**, 613–637.

———, 1889, Die elektromotorische Wirksamkeit der Jonen: Zeitschrift für physikalische Chemie, **4**, 129–181.

O'Konski, C. T., 1960, Electric properties of macromolecules. v. theory of ionic polarization in polyelectrolytes: The Journal of Physical Chemistry, **64**, 605–619.

Placencia-Gómez, E., and L. D. Slater, 2014, Electrochemical spectral induced polarization modeling of artificial sulfide-sand mixtures: Geophysics, **79**, EN91–EN106.

———, 2015, On the pore water chemistry effect on spectral induced polarization measurements in the presence of pyrite: Journal of Applied Geophysics.

Planck, M., 1890, Ueber die Erregung von Electricität und Wärme in Electrolyten: Annalen der Physik, **275**, 161–186.

Revil, A., G. Z. Abdel Aal, E. A. Atekwana, D. Mao, and N. Florsch, 2015a, Induced polarization response of porous media with metallic particlespart 2: Comparison with a broad database of experimental data: Geophysics, **80**, D539–D552.

Revil, A., N. Florsch, and D. Mao, 2015b, Induced polarization response of porous media with metallic particlespart 1: A theory for disseminated semiconductors: Geophysics, **80**, D525–D538.

Reyes-Bozo, L., M. Escudey, E. Vyhmeister, P. Higueras, A. Godoy-Faúndez, J. L. Salazar, H. Valdés-González, G. Wolf-Sepúlveda, and R. Herrera-Urbina, 2015, Adsorption of biosolids and their main components on chalcopyrite, molybdenite and pyrite: Zeta potential and ftir spectroscopy studies: Minerals Engineering, **78**, 128–135.

Schurr, J., 1964, On the theory of the dielectric dispersion of spherical colloidal particles in electrolyte solution1: The Journal of Physical Chemistry, **68**, 2407–2413.

Schwarz, G., 1962, A theory of the low-frequency dielectric dispersion of colloidal particles in electrolyte solution1, 2: The Journal of Physical Chemistry, **66**, 2636–2642.

Shi, Z., D. Fan, R. L. Johnson, P. G. Tratnyek, J. T. Nurmi, Y. Wu, and K. H. Williams, 2015, Methods for characterizing the fate and effects of nano zerovalent iron during groundwater remediation: Journal of contaminant hydrology, **181**, 17–35.

Shilov, V., A. Delgado, F. Gonzalez-Caballero, and C. Grosse, 2001, Thin double layer theory of the wide-frequency range dielectric dispersion of suspensions of non-conducting spherical particles including surface conductivity of the stagnant layer: Colloids and Surfaces A: Physicochemical and Engineering Aspects, **192**, 253–265.

Sund, J., H. Alenius, M. Vippola, K. Savolainen, and A. Puustinen, 2011, Proteomic characterization of engineered nanomaterial–protein interactions in relation to surface reactivity: Acs Nano, **5**, 4300–4309.

Wong, J., 1979, An electrochemical model of the induced-polarization phenomenon in disseminated sulfide ores: Geophysics, **44**, 1245–1265.

Wong, J., and D. Strangway, 1981, Induced polarization in disseminated sulfide ores containing elongated mineralization: Geophysics, **46**, 1258–1268.

LIST OF FIGURES

1 Three-dimensional sketch of the modelled volume. The spherical particle of radius a is enclosed by a cylinder of radius L and height $2L$ representing the surrounding electrolyte solution. Red lines mark the actual two-dimensional model domain discretized for the numerical simulation. Due to the particular set of boundary conditions on the surface of the particle, it is not necessary to model any of the perturbation quantities in its interior.

2 Static diffuse layer (first row) and field-induced perturbations around a sub-micron particle with $a = 0.1$ μm at the low-frequency limit $\omega = 3 \cdot 10^4$ rad/s (other four rows). Only the real parts of the complex-valued perturbation quantities are illustrated; the respective imaginary parts are much smaller at the low-frequency limit displayed here. The inner dashed line indicates the diffuse layer, the outer the volume-diffusion layer. All remaining parameters as listed in Table 1.

3 Radial profiles ($y = 0$, $x > 0$) of the real parts of the perturbation concentrations of (a) anions, (b) active, and (c) passive cations at $\omega = 3 \cdot 10^4$ rad/s. For $\zeta = 0$, numerical results (filled circles) are plotted along with the respective analytical solutions (solid lines) from Bücker et al. (2018). For $\zeta < 0$, only numerical results (open symbols, dashed lines) exist. For both cases, results without (grey) and with (black) reaction current are displayed. The vertical dashed lines indicate the extensions of the diffuse layer (DL, left line) and of the volume-diffusion layer (right line). All other parameter values as in Table 1.

4 Radial profiles ($y = 0$, $x > 0$) of the real parts of the perturbation concentrations of (a) anions, (b) active, and (c) passive cations in the vicinity of a conducting sphere of radius $a = 10$ mm at $\omega = 10^{-4}$ rad/s. For $\zeta = 0$, numerical results (filled circles) are plotted along with the respective analytical solutions (solid lines) from Bücker et al. (2018). For $\zeta < 0$, only numerical results (open symbols, dashed lines) exist. For both cases, results

without (grey) and with (black) reaction current are displayed. The vertical dashed lines indicate the extensions of the diffuse layer (DL, left line) and of the volume-diffusion layer (right line). All other parameter values as in Table 1.

5 Radial profiles ($y = 0$, $x > 0$) of the real part of the perturbation potential in the vicinity of conducting spheres (a) of radius $a = 0.1$ μm at $\omega = 3 \cdot 10^4$ rad/s and (b) of radius $a = 10$ mm at $\omega = 10^{-4}$ rad/s. For $\zeta = 0$, numerical results (filled circles) are plotted along with the respective analytical solutions (solid lines) from Bücker et al. (2018). For $\zeta < 0$, only numerical results (open symbols, dashed lines) exist. For both cases, results without (grey) and with (black) reaction current are displayed. The potential $-E_0 x$ associated with the uniform external field $\mathbf{E}_{\text{ext}}$ as well as the potentials around a non-conducting ($f = -1/2$) and a perfectly conducting ($f = 1$) sphere are also included. The vertical dashed lines indicate the extensions of the diffuse layer (DL, left line) and the volume-diffusion layer (right line). All other parameter values as in Table 1

6 Variation of real (σ', top) and imaginary (σ'', bottom) part of the effective normalized conductivity with angular frequency. For the uncharged particle ($\zeta = 0$), numerical spectra (filled circles) can be compared to the analytical solution (solid lines) from Wong (1979). For the charged particle ($\zeta < 0$), only numerical spectra (open symbols, dashed lines) exist. For both uncharged and charged particles, spectra without (grey) and with (black) reaction currents are displayed. All other parameter values as in Table 1.

7 As Figure 6 but for larger particle with $a = 10$ mm.

8 Variation of the low-frequency limit of the effective conductivity σ_{DC} (left panel) and the maximum imaginary conductivity σ''_{max} (right panel) with the ζ-potential for radii $a = 0.1$ μm, 31.6 μm (left and right panel), and 10 mm (right panel only). Conductivity variations are displayed for simulations with (black circles) and without (grey diamonds)

reaction currents. The black solid lines illustrate the analytical approximation of σ_{DC} based on the surface conductivity according to O'Konski (1960). Besides a and ζ, all parameter values as in Table 1.

9 Variation of relaxation times τ with particle radius a for three different concentrations of active anions $n_3^\infty = 0, 0.03$, and 0.12 mol/m^3 (light grey, dark grey, and black, respectively). For the uncharged particle ($\zeta = 0$), numerical results (filled circles) can be compared to the analytical solution (solid lines) from Wong (1979). For the charged particle ($\zeta < 0$), only numerical results (open symbols, dashed lines) can be displayed. Beside a, ζ, and n_3^∞, all other parameters as in Table 1.

10 Variation of relaxation times τ with the ζ-potential for three different particle radii $a = 10^{-7}, 3.16 \cdot 10^{-5}$, and 10^{-2} m with (black) and without (grey) reaction currents. All other parameter values are equal to those given in Table 1.

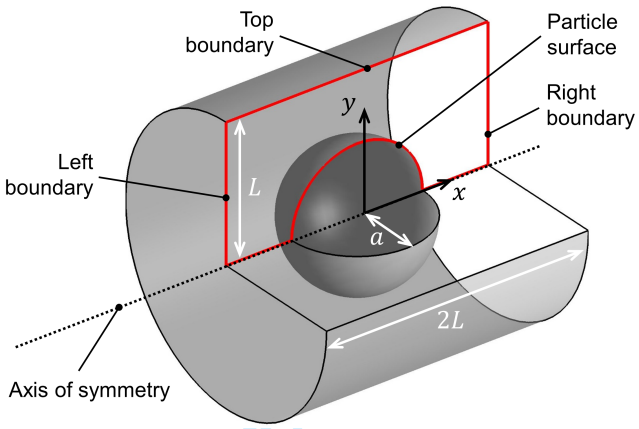

Figure 1: Three-dimensional sketch of the modelled volume. The spherical particle of radius a is enclosed by a cylinder of radius L and height $2L$ representing the surrounding electrolyte solution. Red lines mark the actual two-dimensional model domain discretized for the numerical simulation. Due to the particular set of boundary conditions on the surface of the particle, it is not necessary to model any of the perturbation quantities in its interior.

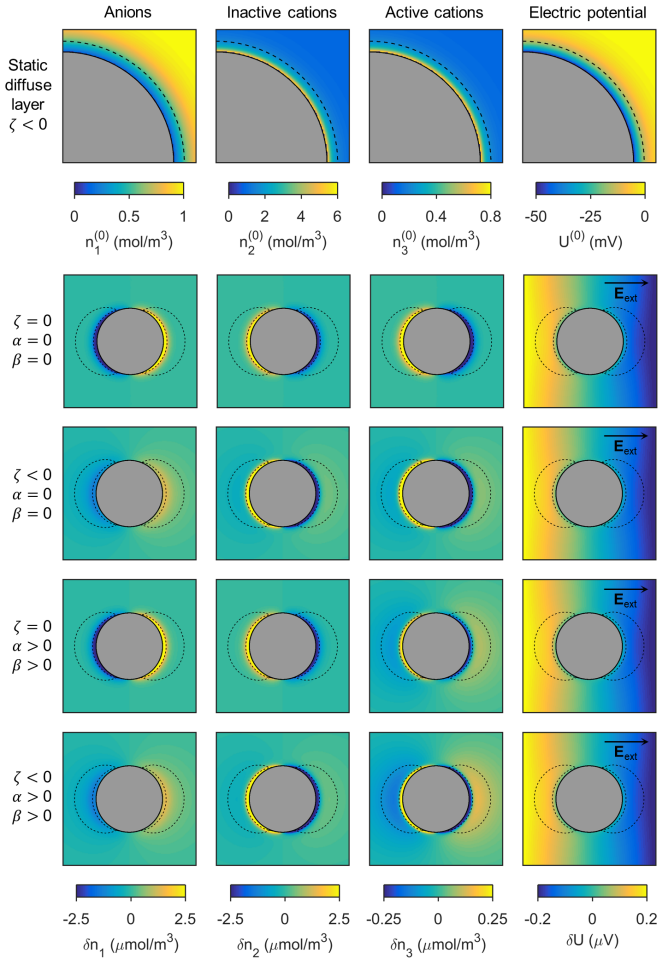

Figure 2: Static diffuse layer (first row) and field-induced perturbations around a submicron particle with $a = 0.1$ μm at the low-frequency limit $\omega = 3 \cdot 10^4$ rad/s (other four rows). Only the real parts of the complex-valued perturbation quantities are illustrated; the respective imaginary parts are much smaller at the low-frequency limit displayed here. The inner dashed line indicates the diffuse layer, the outer the volume-diffusion layer. All remaining parameters as listed in Table 1.

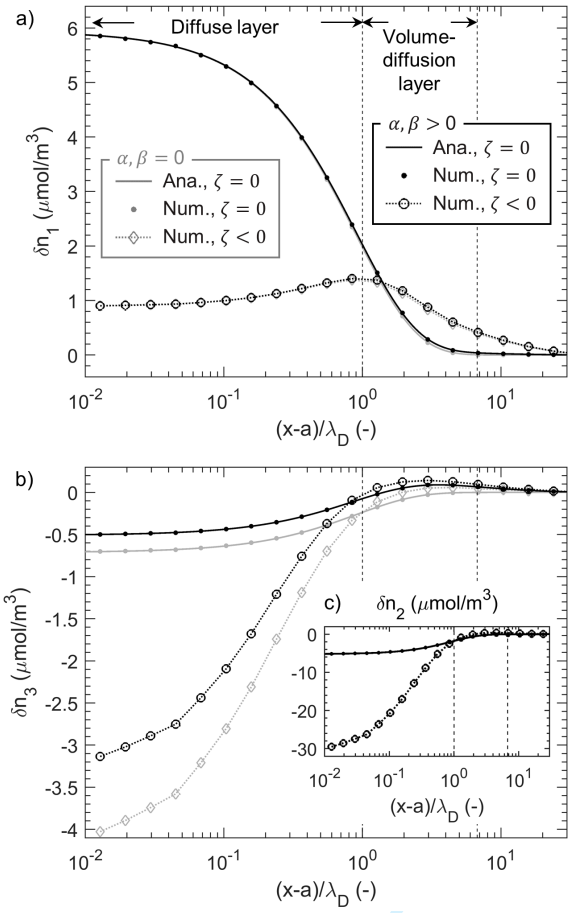

Figure 3: Radial profiles ($y = 0$, $x > 0$) of the real parts of the perturbation concentrations of (a) anions, (b) active, and (c) passive cations at $\omega = 3 \cdot 10^4$ rad/s. For $\zeta = 0$, numerical results (filled circles) are plotted along with the respective analytical solutions (solid lines) from Bücker et al. (2018). For $\zeta < 0$, only numerical results (open symbols, dashed lines) exist. For both cases, results without (grey) and with (black) reaction current are displayed. The vertical dashed lines indicate the extensions of the diffuse layer (DL, left line) and of the volume-diffusion layer (right line). All other parameter values as in Table 1.

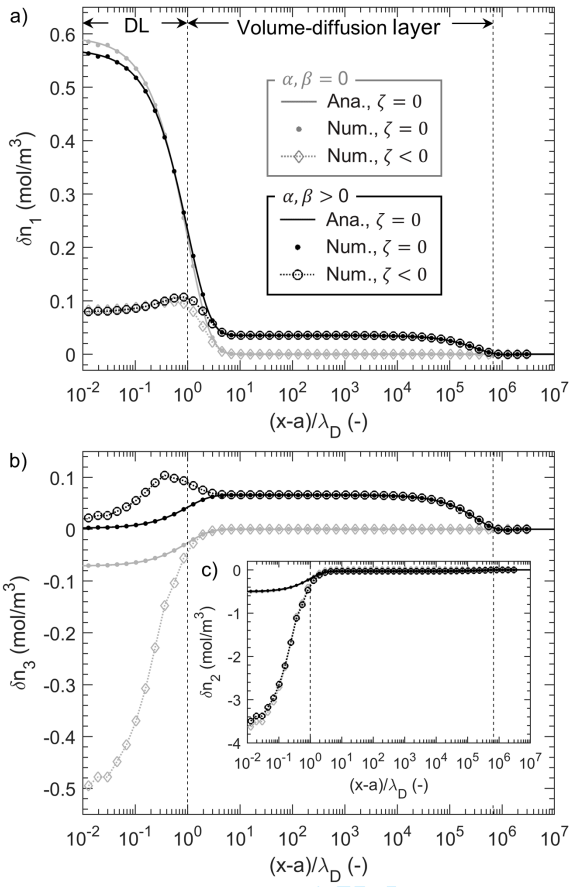

Figure 4: Radial profiles ($y = 0$, $x > 0$) of the real parts of the perturbation concentrations of (a) anions, (b) active, and (c) passive cations in the vicinity of a conducting sphere of radius $a = 10$ mm at $\omega = 10^{-4}$ rad/s. For $\zeta = 0$, numerical results (filled circles) are plotted along with the respective analytical solutions (solid lines) from Bücker et al. (2018). For $\zeta < 0$, only numerical results (open symbols, dashed lines) exist. For both cases, results without (grey) and with (black) reaction current are displayed. The vertical dashed lines indicate the extensions of the diffuse layer (DL, left line) and of the volume-diffusion layer (right line). All other parameter values as in Table 1.

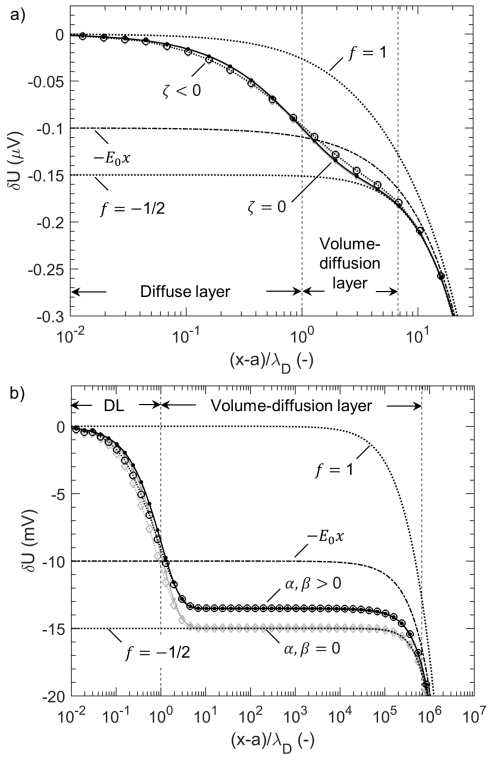

Figure 5: Radial profiles ($y = 0$, $x > 0$) of the real part of the perturbation potential in the vicinity of conducting spheres (a) of radius $a = 0.1$ μm at $\omega = 3 \cdot 10^4$ rad/s and (b) of radius $a = 10$ mm at $\omega = 10^{-4}$ rad/s. For $\zeta = 0$, numerical results (filled circles) are plotted along with the respective analytical solutions (solid lines) from Bücker et al. (2018). For $\zeta < 0$, only numerical results (open symbols, dashed lines) exist. For both cases, results without (grey) and with (black) reaction current are displayed. The potential $-E_0x$ associated with the uniform external field $\mathbf{E}_{\text{ext}}$ as well as the potentials around a non-conducting ($f = -1/2$) and a perfectly conducting ($f = 1$) sphere are also included. The vertical dashed lines indicate the extensions of the diffuse layer (DL, left line) and the volume-diffusion layer (right line). All other parameter values as in Table 1

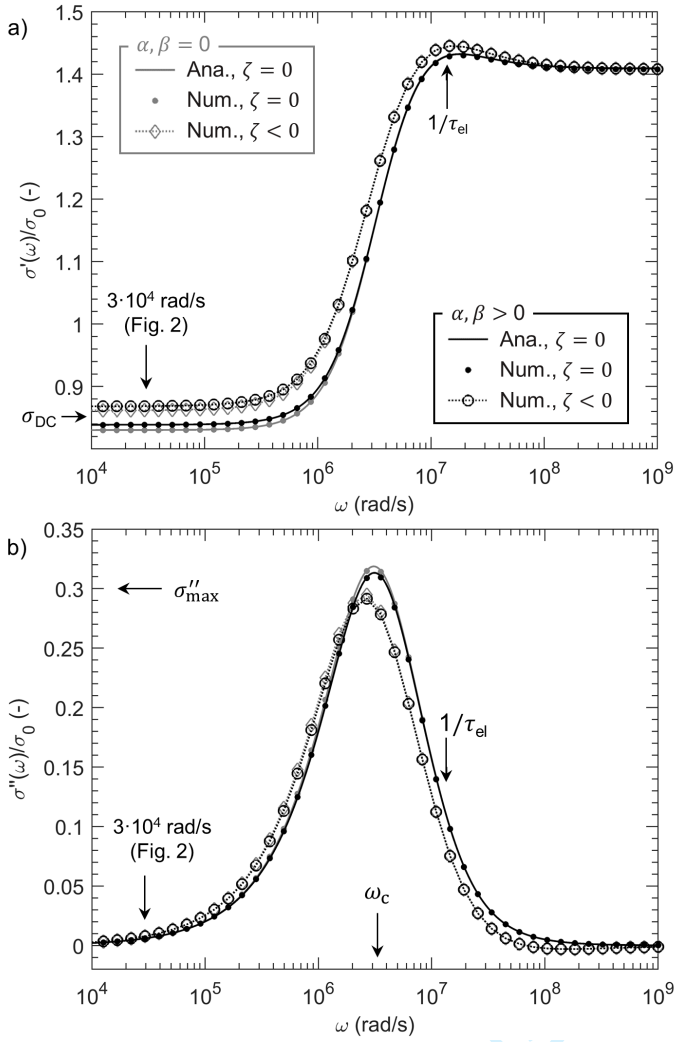

Figure 6: Variation of real (σ', top) and imaginary (σ'', bottom) part of the effective normalized conductivity with angular frequency. For the uncharged particle ($\zeta = 0$), numerical spectra (filled circles) can be compared to the analytical solution (solid lines) from Wong (1979). For the charged particle ($\zeta < 0$), only numerical spectra (open symbols, dashed lines) exist. For both uncharged and charged particles, spectra without (grey) and with (black) reaction currents are displayed. All other parameter values as in Table 1.

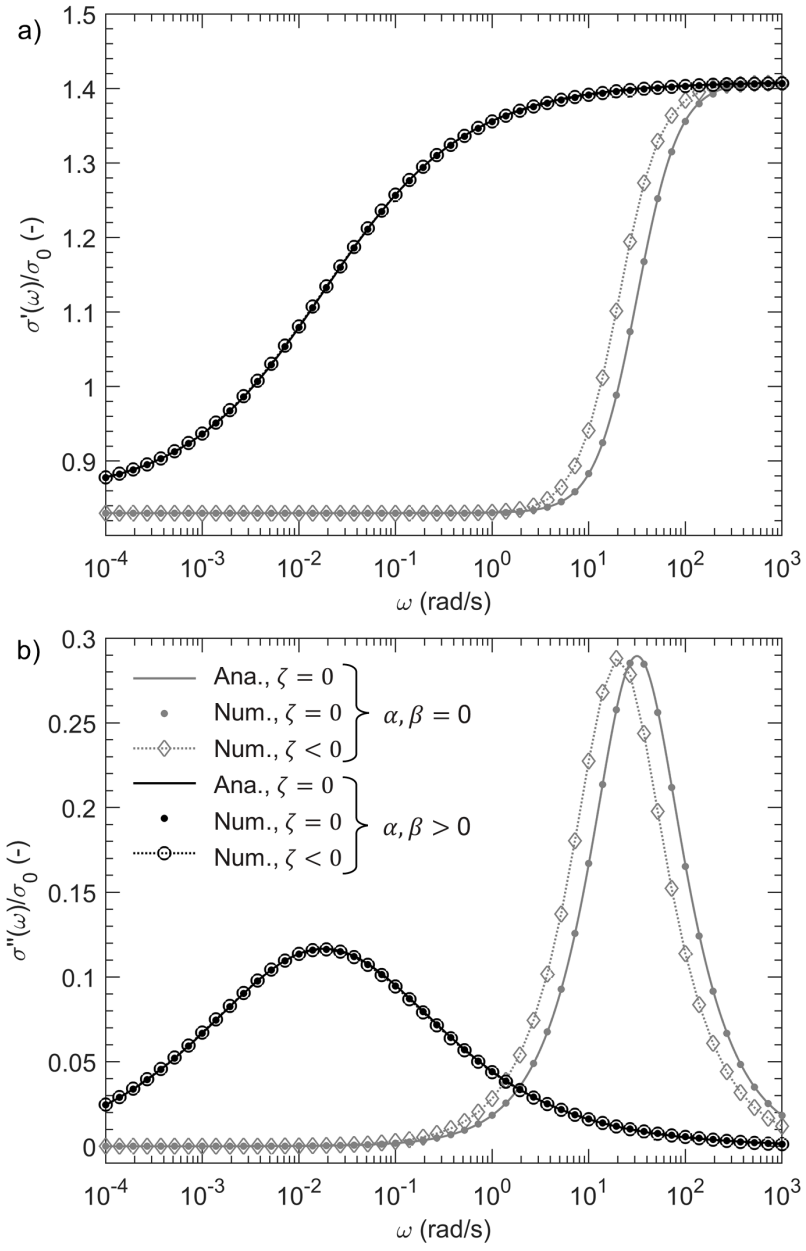

Figure 7: As Figure 6 but for larger particle with $a = 10$ mm.

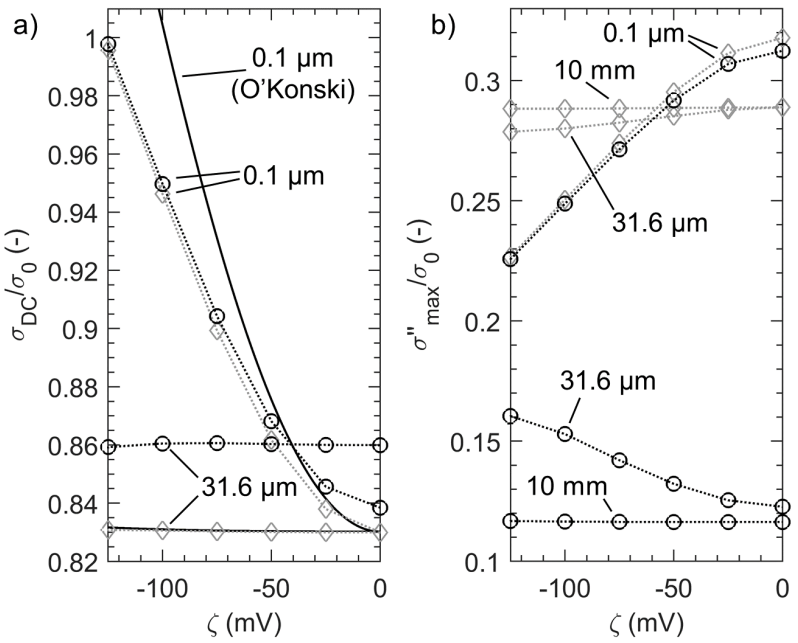

Figure 8: Variation of the low-frequency limit of the effective conductivity σ_{DC} (left panel) and the maximum imaginary conductivity σ''_{max} (right panel) with the ζ-potential for radii $a = 0.1$ μm, 31.6 μm (left and right panel), and 10 mm (right panel only). Conductivity variations are displayed for simulations with (black circles) and without (grey diamonds) reaction currents. The black solid lines illustrate the analytical approximation of σ_{DC} based on the surface conductivity according to O'Konski (1960). Besides a and ζ, all parameter values as in Table 1.

–

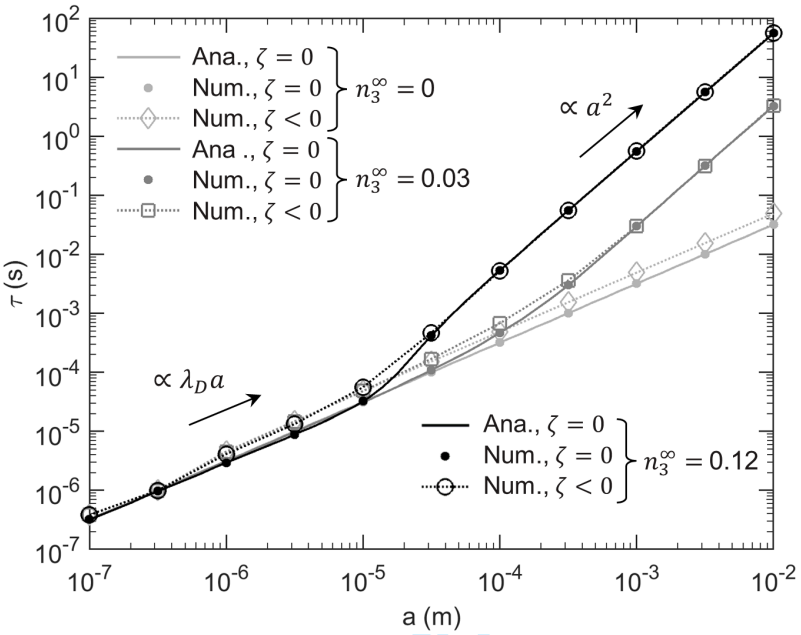

Figure 9: Variation of relaxation times τ with particle radius a for three different concentrations of active anions $n_3^\infty = 0, 0.03$, and 0.12 mol/m^3 (light grey, dark grey, and black, respectively). For the uncharged particle ($\zeta = 0$), numerical results (filled circles) can be compared to the analytical solution (solid lines) from Wong (1979). For the charged particle ($\zeta < 0$), only numerical results (open symbols, dashed lines) can be displayed. Beside a, ζ, and n_3^∞, all other parameters as in Table 1.

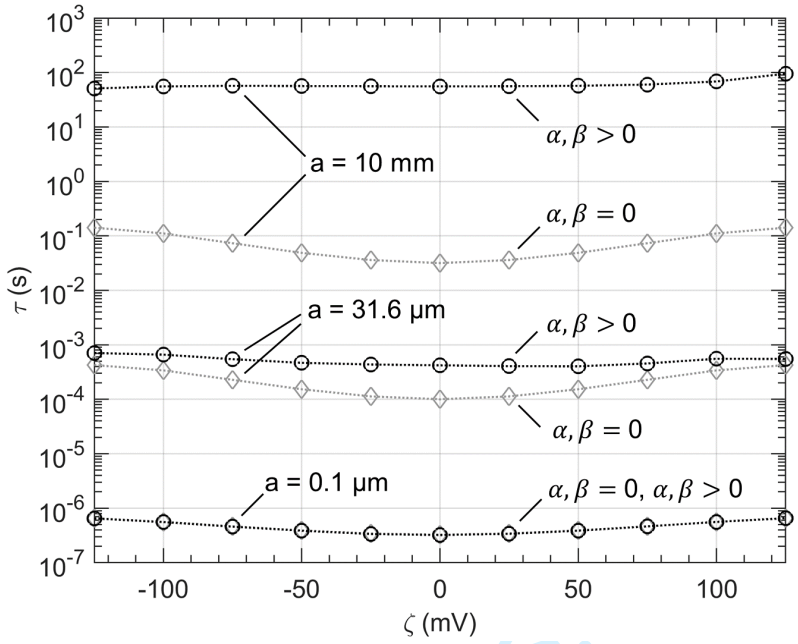

Figure 10: Variation of relaxation times τ with the ζ-potential for three different particle radii $a = 10^{-7}, 3.16 \cdot 10^{-5}$, and 10^{-2} m with (black) and without (grey) reaction currents. All other parameter values are equal to those given in Table 1.